Digital-analog simulations of Schrödinger cat states in the Dicke-Ising model

Dmitriy S. Shapiro [1,*] Yannik Weber [2] Tim Bode,[1] Frank K. Wilhelm [1,2] and Dmitry Bagrets [1,3]

[1]*Peter Grünberg Institute, Quantum Computing Analytics (PGI-12), Forschungszentrum Jülich, 52425 Jülich, Germany*

[2]*Theoretical Physics, Universität des Saarlandes, 66123 Saarbrücken, Germany*

[3]*Institute for Theoretical Physics, University of Cologne, 50937 Köln, Germany*

(Received 19 December 2024; revised 29 July 2025; accepted 16 September 2025; published 6 October 2025)

The Dicke-Ising model, one of the few paradigmatic models of matter-light interaction, exhibits a superradiant quantum phase transition above a critical coupling strength. However, in natural optical systems, its experimental validation is hindered by a "no-go theorem." Here, we propose a digital-analog quantum simulator for this model based on an ensemble of interacting qubits coupled to a single-mode photonic resonator. We analyze the system's free-energy landscape using field-theoretical methods and develop a digital-analog quantum algorithm that disentangles qubit and photon degrees of freedom through a parity-measurement protocol. This disentangling enables the emulation of a photonic Schrödinger cat state, which is a hallmark of the superradiant ground state in finite-size systems and can be unambiguously probed through the Wigner tomography of the resonator's field.

DOI: 10.1103/wbp6-y3vd

I. INTRODUCTION

The Dicke-Ising model has garnered significant attention in recent years due to the richness of its quantum phases [1–8]. A central feature of this model is the competition between spin-spin interactions, which tend to drive an Ising transition, and the collective Dicke coupling, which leads to superradiant photon condensation. This interplay results in a more complex superradiant quantum phase transition (QPT) compared to that in the conventional Dicke model [9–15].

In natural optical systems, the superradiant QPT is generally considered forbidden by a no-go theorem, which asserts that the diamagnetic term, proportional to the square of the vector potential $\hat{\mathbf{A}}^2$, prevents photon condensation. However, this constraint can be circumvented [16–18] in quantum simulators such as cold-atom lattices [19–26] or circuit QED setups [27–29] (see also review articles [30–33]), where the theorem is overcome on the physical level.

Another possibility to simulate the class of Dicke-type models could potentially be offered by quantum hardware, which relies on the Trotterized approximation of the evolution operator via quantum circuits. This approach, known as digital quantum simulation [34–39], has recently become a popular line of research and is considered one of the few promising future applications of quantum computers. Its validity has been successfully verified in numerous experiments (see recent reviews such as Ref. [40]). However, simulating many-body correlated systems with spin-boson or fermion-boson interactions presents a distinct challenge: encoding bosonic fields using qubits. Specifically, encoding a single bosonic mode with a finite occupation-number cutoff $N_{\max}$ requires $\log_2 N_{\max}$ qubits [41,42]. To address this problem, one may work within the alternative quantum digital-analog framework [43,44]. The latter employs bosonic degrees of freedom as a computational resource and enables boson-qubit entanglement at the hardware level. Within this scheme, the dynamics of the quantum Rabi model in the strongly coupled limit was simulated using a single transmon qubit coupled to a resonator [44]. More recently, this concept has been suggested for simulating the lattice gauge theories [45] and Hubbard-Holstein model [46]. Our study leverages this methodology to simulate the dynamics governed by the more elaborate Dicke-Ising Hamiltonian, with a focus on novel qubit-boson architectures that are experimentally feasible within the context of circuit QED [44,47]. Superconducting platforms are particularly well suited for this purpose due to the long coherence times of their resonators (on the order up to milliseconds [48,49]), which significantly exceed the timescales of analog evolution (hundred of nanoseconds [44]). In contrast, implementing alternative systems such as trapped ions coupled to vibrational modes is more challenging in this regard. The decay time (on the order of tens of milliseconds) are only about two orders of magnitude greater than the relevant Rabi periods [50,51].

A particularly compelling aspect of our digital-analog approach is twofold: (i) the potential to simulate the transition into the superradiant phase via a quench protocol, and (ii) the ability to disentangle the photon condensate and the qubit degrees of freedom in the many-body density matrix. This gives the proposed simulation strategy a striking advantage over fully analog simulators [23], where only macroscopic parameters of the condensate have been available for direct measurement. Remarkably, this disentanglement of condensed photons can enable the emulation of Schrödinger

*Contact author: d.shapiro@fz-juelich.de

cat states, which are a hallmark of the superradiant ground state in finite-size systems.

The paper is organized as follows. In Sec. II, we present the model and the main idea of creating a cat-state density matrix with the help of qubit-parity measurements. In Sec. III, we provide a field-theory description of the superradiant QPT for different limits of the model. We introduce the method of deriving the free energy using path integrals in Sec. III A. The mean-field results for the conventional Dicke model and the Dicke-Ising model with spin $\frac{1}{2}$ are discussed in Secs. III B and III C, respectively. The role of quantum fluctuations near the instanton trajectory and the relation to the Kibble-Zurek mechanism are addressed in Sec. III D. The generalization of the Dicke-Ising model to spins larger than $\frac{1}{2}$, via angular bosonization, is provided in Sec. III E. A quasiclassical approach for angular fluctuations is presented in Sec. III F. In Sec. IV, we present the quantum simulation algorithm. We discuss the idea of the superradiant ground-state approximation via the quench in Sec. IV A. In Sec. IV B, we present digital-analog quantum circuits for Jaynes-Cummings, Rabi, and Dicke gates; in Sec. IV C we give an overview of the algorithm. In Sec. V, we discuss our results and present data for the exact and Trotterized dynamics; in the ending Sec. VI we conclude.

II. MAIN IDEA

The Dicke-Ising model ($\hbar = k_B = 1$ hereafter),

$$\hat{H}_{\rm DI} = \hat{H}_{\rm D} - J\sum_{j=1}^{N-1}\hat{\sigma}_j^z\hat{\sigma}_{j+1}^z, \tag{1}$$

is a combination of the standard Ising model and the Dicke Hamiltonian

$$\hat{H}_{\rm D} = \omega_0\hat{a}^\dagger\hat{a} - \omega_z\sum_{j=1}^{N}\hat{\sigma}_j^z + \frac{g}{\sqrt{N}}(\hat{a}^\dagger + \hat{a})\sum_{j=1}^{N}\hat{\sigma}_j^x, \tag{2}$$

which describes an ensemble of N spin-s degrees of freedom coupled to a common photon mode. In the Ising part of Eq. (1), a positive coupling $J > 0$ corresponds to a ferromagnetic spin-spin interaction. Through the Dicke part of Eq. (1), the spins obtain excitation frequencies $\omega_z > 0$, while the photon mode has frequency ω_0 and is described by the bosonic annihilation and creation operators, $\hat{a}$ and $\hat{a}^\dagger$, commuting as $[\hat{a}, \hat{a}^\dagger] = 1$ and acting in the space of photonic Fock states $|n\rangle$ as $\hat{a}|n\rangle = \sqrt{n}|n-1\rangle$ and $\hat{a}^\dagger|n\rangle = \sqrt{n+1}|n+1\rangle$ with n being a photon number; the qubit-resonator coupling strength is denoted by g. For qubits, which correspond to spin $s = \frac{1}{2}$, we associate the logical $|0\rangle_j$ of qubit $j = 1, \ldots, N$ to the eigenstate $(1, 0)^T$ of $\hat{\sigma}_j^z$ with the eigenvalue 1.

At zero temperature, g plays the role of a control parameter of the superradiant QPT. If g is less than the critical value g_c, the system is in its normal phase, with a *ferromagnetic* ground state

$$|{\rm FM}\rangle = |0\rangle\otimes\prod_{j=1}^{N}|0_j\rangle. \tag{3}$$

In the *superradiant* phase, where $g > g_c$, there exist two quasidegenerate superradiant many-body states $|\Psi_R\rangle$ and $|\Psi_L\rangle$, and the highly entangled ground state becomes the superposition

$$|{\rm SR}\rangle = \frac{1}{\sqrt{2}}(|\Psi_L\rangle + |\Psi_R\rangle). \tag{4}$$

In a large spin ensemble, these wave functions are given by the direct products $|\Psi_R\rangle = |-\alpha\rangle\otimes|R\rangle$ and $|\Psi_L\rangle = |\alpha\rangle\otimes|L\rangle$. Here, $|\pm\alpha\rangle = e^{-\frac{1}{2}|\alpha|^2}\sum_{n\geqslant 0}\frac{(\pm\alpha)^n}{\sqrt{n!}}|n\rangle$ are photon coherent states with opposite phases. The number of photons stored in these states, $|\alpha|^2$, can be macroscopically large. In the mean-field picture, the value of α is given by a free-energy minimum. The qubit states $|R(L)\rangle = \prod_{j=1}^{N}(|0\rangle_j \pm |1\rangle_j)/\sqrt{2}$ are antiparallel to each other (on their respective single-particle Bloch spheres).

Let us remember that in circuit QED, Schrödinger's cat state is the nonclassical state

$$|{\rm cat}\rangle = \frac{1}{\sqrt{2}}(|\alpha\rangle + |-\alpha\rangle), \tag{5}$$

which is a promising candidate for qubit encoding due to its nonlocality in phase space [53–56], rendering it stable against local perturbations provided the photon number is large.

The central idea of our work is to disentangle $|\pm\alpha\rangle$ and $|R(L)\rangle$ from the joint many-body density matrix, $\hat{\rho}_{\rm SR} = |{\rm SR}\rangle\langle{\rm SR}|$, thus emulating the cat-state density matrix in the photon basis, i.e.,

$$\hat{\rho}_{\rm cat} = \tfrac{1}{2}(|-\alpha\rangle\langle-\alpha| + |\alpha\rangle\langle\alpha| + |\alpha\rangle\langle-\alpha| + |-\alpha\rangle\langle\alpha|). \tag{6}$$

Note that simply taking the trace over the qubit degrees of freedom in $\hat{\rho}_{\rm SR}$ results in a mixed-state density matrix

$$\hat{\rho}_{\rm mix} = {\rm tr}_\sigma[\hat{\rho}_{\rm SR}] = \tfrac{1}{2}(|-\alpha\rangle\langle-\alpha| + |\alpha\rangle\langle\alpha|), \tag{7}$$

which lacks the coherent cross terms $|\pm\alpha\rangle\langle\mp\alpha|$ that appear in Eq. (6). To obtain these cross terms, we select one half of the qubit states corresponding to a given value of the total qubit parity. This selective parity measurement can be defined as

$$\hat{\rho}_+ = {\rm tr}_\sigma[\hat{\rho}_{\rm SR}\hat{P}_+], \tag{8}$$

where the positive parity operator is

$$\hat{P}_+ = \frac{1}{2}\left(\hat{1} + \prod_{j=1}^{N}\hat{\sigma}_j^z\right), \tag{9}$$

with $\hat{P}_+|R\rangle = \hat{P}_+|L\rangle = (|R\rangle + |L\rangle)/\sqrt{2}$. The trace with the $\hat{P}_+$ in Eq. (8) provides the desired result, i.e., $\hat{\rho}_+ = \hat{\rho}_{\rm cat}$. Performing a series of projective measurements following Eq. (8) enables us to observe nonclassical cat-state signatures in a subsequent Wigner tomography [53,54] of the photon mode.

Consider the Wigner function $W(x, p)$ corresponding to a reduced density matrix $\hat{\rho} = {\rm tr}_\sigma[\hat{\mathcal{O}}\hat{\rho}_{\rm SR}]$,

$$W(x, p) = \sum_{n,m=0}^{\infty}\langle n|\hat{\rho}|m\rangle V_{n,m}(x, p), \tag{10}$$

where

$$V_{n,m}(x, p) = \int dy\frac{H_n(x-y)H_m(x+y)e^{2ipy-(x^2+y^2)}}{\sqrt{\pi\, 2^{n+m}n!m!}} \tag{11}$$

are the harmonic oscillator eigenfunctions overlap integrals, and $H_n(x) = (-1)^n e^{x^2}d^n e^{-x^2}/dx^n$ are Hermite polynomials.

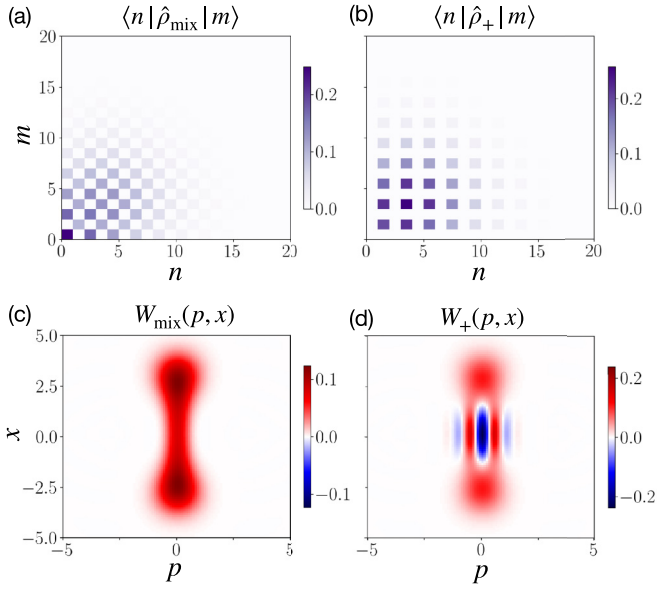

FIG. 1. Reduced density matrices (a) for the mixed state $\hat{\rho}_{\rm mix} = {\rm tr}_\sigma[\hat{\rho}_{\rm SR}]$ and (b) when projected to the positive-parity subspace $\hat{\rho}_+ = {\rm tr}_\sigma[\hat{\rho}_{\rm SR}\hat{P}_+]$. (c) Wigner function of the mixed state, and (d) of the projected state showing nonclassical features indicative of a cat state. The photon Hilbert space has a cutoff of 20 photons. The coupling $g = 0.9\sqrt{\omega_0 J}$ is near the critical value $\tilde{g}_{\rm c}$, the chain has open ends and comprises $N = 7$ qubits. The other parameters are $J = \omega_0$ and $\omega_z = 0.05\omega_0$.

Following to the definitions (7) and (8), we have $\hat{\mathcal{O}} = \hat{1}$ for the mixed state and $\hat{\mathcal{O}} = \hat{P}_+$ for the cat state.

The momentum-integrated Wigner function yields the photon probability distribution $w(x) = \int dp\, W(x,p)$, which reduces to

$$w(x,t) = e^{-x^2} \sum_{n,m\geqslant 0} \frac{H_n(x)H_m(x)}{\sqrt{\pi 2^{n+m} n!m!}} \langle n|\hat{\rho}(t)|m\rangle. \tag{12}$$

In Figs. 1(a) and 1(b) we present, respectively, illustrations of the matrix elements of $\hat{\rho}_{\rm mix}$ and $\hat{\rho}_+$ for a finite system in the superradiant phase. The many-body density matrix $\hat{\rho}_{\rm SR}$ is found numerically via exact diagonalization of the Dicke-Ising Hamiltonian. One can observe that $\langle n|\hat{\rho}|m\rangle \neq 0$ if both of Fock state numbers n, m are odd. In the thermodynamic limit, $W_{\rm mix}(x,p)$ would have two singular points at $x = \pm\sqrt{2}\alpha$; in a finite system near the critical point, $W_{\rm mix}(x,p)$ has two linked blobs as shown in Fig. 1(c).

The projected Wigner function $W_+(x,p)$ calculated from $\hat{\rho}_+$ is shown in Fig. 1(d). The signatures of Schrödinger's cat state are visible as fringes of negative quasiprobability $W_+(x,p)<0$, which is a benchmark for the presence of cat states in the output of our algorithm given below.

We note that the Wigner function for negative parity $W_- = W_{\rm mix} - W_+$, where the corresponding projector is $\hat{P}_- = \hat{1} - \hat{P}_+$, also exhibits cat-state signatures, albeit less prominently. The choice of positive parity in our protocol follows from the fact that in the $g = 0$ limit, the system has positive parity (i.e., $\langle \hat{P}_+\rangle = 1$ and $\langle \hat{P}_-\rangle = 0$), which is a feature of the normal *ferromagnetic* state supported by $J > 0$ and $\omega_z > 0$. Near the critical coupling $g_{\rm c}$, or under quench dynamics, the system becomes partially superradiant *paramagnetic*, and the expectation value satisfies $\frac{1}{2} < \langle \hat{P}_+\rangle < 1$. Deep in the superradiant phase, $\langle \hat{P}_+\rangle$ and $\langle \hat{P}_-\rangle$ approach $\frac{1}{2}$, indicating that the probabilities to observe positive and negative parity become balanced.

The remainder of the paper has two main threads: (i) Applying methods of statistical physics to derive a profile of the free energy. This sheds light on the order of the QPT as well as on the quantum fluctuations around the mean-field solutions and the associated macroscopic quantum tunneling between the superradiant states $|\Psi_L\rangle$ and $|\Psi_R\rangle$. (ii) Based on this understanding of the free-energy profile, we then perform quantum-circuit simulations of the real-time dynamics of the photon distribution in the corresponding effective potential, culminating in the sought-for cat states.

III. SUPERRADIANT QUANTUM PHASE TRANSITIONS

In this section, we start with a recapitulation of the well-known result about the second-order QPT in the conventional Dicke model. After that, we turn to the Dicke-Ising Hamiltonian (1) with $J \neq 0$ and $\omega_z = 0$; the limit $\omega_z \to 0$ enables an exact calculation of the trace over the spins. It can be performed for qubits ($s = \frac{1}{2}$) via the usual Jordan-Wigner transformation, resulting in a mean-field solution for the free energy that predicts a first-order QPT. Aside from that, the free energy determines an instanton trajectory in Matsubara imaginary time and, therefore, the rate of macroscopic quantum tunneling.

For $\omega_z \ll J$, in the superradiant phase, the order-parameter fluctuations are critical because the magnon excitations become gapless [Eq. (22)]. If the fluctuations are unstable, the Gaussian approximation is not sufficient. If s is large (qudit case), and the photon mode has a low frequency, then fluctuations are suppressed; the mean-field solution becomes asymptotically exact in this case. At finite $\omega_z \sim J$, integrating out the magnons exactly via the Jordan-Wigner transformation is more challenging. As an alternative approach, we therefore suggest the angular representation of spins, which is valid for arbitrary s.

A. Methods

To calculate the free energy F as a function of the superradiant order parameter, we recall the relation between F and the partition function $Z = {\rm tr}e^{-\hat{H}/T}$ at finite temperature T,

$$Z = e^{-F/T}, \tag{13}$$

where the trace is taken over all degrees of freedom. Field-theory methods enable one to represent the trace as a path integral over complex bosonic fields a and $\bar{a}$, while the fields $\vec{\sigma}$ parametrize the spin sector, i.e., the partition function may be written as

$$Z = \int d[a,\bar{a},\vec{\sigma}]e^{-S[a,\bar{a},\vec{\sigma}]}. \tag{14}$$

Upon transformation from a Hamiltonian to the path integral, the real part of the photon operators becomes a trajectory $u(\tau)$

on the Matsubara time interval $\tau \in [0, 1/T]$:

$$\frac{1}{\sqrt{N}}(\hat{a} + \hat{a}^\dagger) \to u(\tau). \tag{15}$$

The trajectories $u(\tau)$ are slow if N is large (thermodynamic limit) and the photon frequency ω_0 is small. This corresponds to the mean-field limit, where u can be associated with the superradiant order parameter. The photon position operator $\hat{x} = \frac{1}{\sqrt{2}}(\hat{a} + \hat{a}^\dagger)$ is related to u by $\hat{x} \to \sqrt{N/2}u$.

The idea now is to calculate the path integral over all *fast* fields and represent the partition function as a single path integral over the *slow* quantum field u, i.e., $Z = \int D[u] \exp(-S_{\rm eff}[u])$; the new functional in the exponential is the effective action for u. The free energy follows from $S_{\rm eff}$ if we neglect the slow time dependence of $u(\tau)$ to obtain

$$F(u) = T S_{\rm eff}[u = \text{const}]. \tag{16}$$

The low-temperature action $S_{\rm eff}$ is proportional to $1/T$; hence, T drops from all the formulas for the free energy.

Note that the momentum operator $\hat{p} = \frac{i}{\sqrt{2}}(\hat{a} - \hat{a}^\dagger)$ does not appear in the interacting part of the Hamiltonian (1). Therefore, in the path integral, the real field v corresponding to $i\hat{p}$ appears only in the free-photon Matsubara action, namely,

$$S_0 = \int_0^{1/T} d\tau\, \bar{a}(\partial_\tau + \omega_0)a, \tag{17}$$

where $a(\tau)$ and $\bar{a}(\tau)$ are complex bosonic fields. If we make a rotation to the real fields $u = (a + \bar{a})/\sqrt{N}$ and $v = i(a - \bar{a})/\sqrt{N}$, and integrate out the field v, we arrive at the free action for the order parameter,

$$S_0[u] = N \int_0^{1/T} d\tau\, \mathcal{L}[u(\tau)], \tag{18}$$

with the Lagrangian

$$\mathcal{L} = \frac{(\partial_\tau u)^2}{4\omega_0} + \frac{\omega_0}{4}u^2. \tag{19}$$

This is the sum of the kinetic term $\sim(\partial_\tau u)^2$ and the potential energy $\mathcal{F}_0 = \omega_0 u^2/4$, which determines the parabolic free-energy profile. In the next section, we show how the interaction with the spins contributes additional terms to $\mathcal{F}$.

B. Free energy in the Dicke model

Consider the conventional Dicke Hamiltonian (2). In what follows, we work with the normalized free energy $\mathcal{F} = F/N$, which, in the thermodynamic limit, reads as

$$\mathcal{F}_{\rm D}(u) = \frac{\omega_0}{4}u^2 - \omega_z\left(\sqrt{1 + \frac{g^2}{\omega_z^2}u^2} - 1\right). \tag{20}$$

This result has been derived by integrating out the qubit states, which can be done via different spin representations such as Holstein-Primakoff bosonization [10] or bilinear combinations of fermion fields [9,11,15]. The Dicke free energy $\mathcal{F}_{\rm D}(u)$ exhibits a second-order QPT, as shown in Figs. 2(a)–2(c). In the normal phase $g < g_{\rm c} = \sqrt{\omega_0\omega_z/2}$ below the critical coupling, there is only one minimum at $u = 0$. At $g = g_{\rm c}$, the QPT occurs. Finally, there is a superradiant phase at $g > g_{\rm c}$,

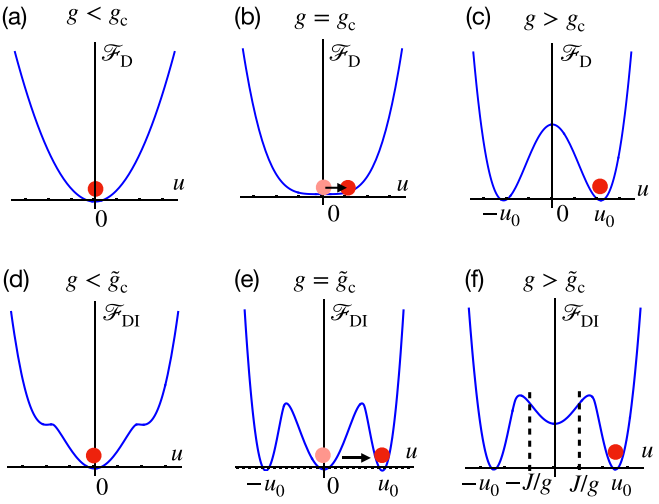

FIG. 2. Sketch of the free energies as functions of the superradiant order parameter for (a)–(c) the Dicke and (d)–(f) the Dicke-Ising models. (a), (d) Normal phases. Critical points (b) of the second-order and (e) first-order QPTs. (d), (f) Superradiant phases. The values $u = \pm J/g$ in (f) correspond to the critical Ising chain.

which means that $\mathcal{F}_{\rm D}(u)$ acquires two minima at $u = \pm u_0$, $u_0 > 0$, and the system spontaneously relaxes to one of them.

C. Free energy in the Dicke-Ising model at $\omega_z = 0$ and $s = \frac{1}{2}$

Coming back to the Dicke-Ising Hamiltonian with $J > 0$, we consider the limit of $\omega_z \to 0$. In Appendix A, we apply the Jordan-Wigner transformation for spin operators and perform the subsequent integral over the fermion fields. As a result, we obtain the mean-field free energy

$$\mathcal{F}_{\rm DI}(u) = \frac{\omega_0}{4}u^2 - \frac{2}{\pi}(g|u| + J)\mathrm{E}\left(\frac{4g|u|J}{(g|u| + J)^2}\right), \tag{21}$$

where the elliptic function $\mathrm{E}(x)$ results from an integral over the quasimomentum in the Brillouin zone $\mathbf{k} \in (-\pi, \pi)$. One obtains two bands of Ising-chain magnons in the Brillouin zone, and their spectrum is

$$\epsilon(\mathbf{k}) = \pm 2\sqrt{g^2u^2(\tau) + J^2 - 2Jgu\cos\mathbf{k}}. \tag{22}$$

In contrast to $\mathcal{F}_{\rm D}$, the function $\mathcal{F}_{\rm DI}$ has three minima in a certain range of g around the critical $\tilde{g}_{\rm c} = c_0\sqrt{\omega_0 J}$, $c_0 \approx 0.9$. The first-order QPT occurs when the two side minima become lower than the central minimum at $u = 0$ [see Figs. 2(d)–2(f)]. Note that our approach is complementary to previous studies of phase transitions in this model [1–8].

D. Instanton approach: Relation to Ising transition and Kibble-Zurek mechanism

The free energy $\mathcal{F}_{\rm DI}$ given by (21) is part of a mean-field Matsubara action where $u(\tau)$ is a trajectory in imaginary time,

$$S_{\rm mf} = N\int_0^{1/T} d\tau\left(\frac{(\partial_\tau u)^2}{4\omega_0} + \mathcal{F}_{\rm DI}(u)\right). \tag{23}$$

Variation of this action yields an instanton equation that describes macroscopic quantum tunneling between the minima

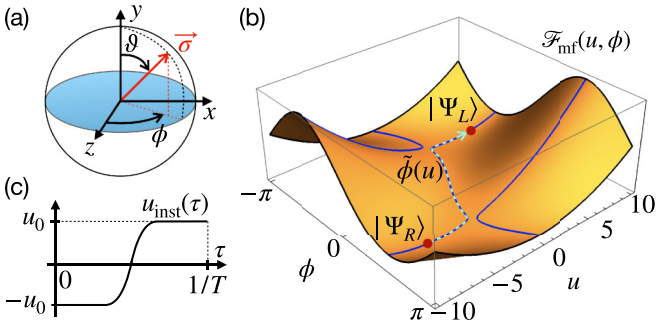

FIG. 3. (a) Angular representation of qubit states. The xz plane contributing most to the mean-field solution is shown in blue. (b) The effective potential in the mean-field approximation. The red dots are the two minima representing the superradiant states $|\Psi_{R,L}\rangle$. The dashed curve is an instanton trajectory. (c) Schematic representation of the instanton trajectory $u_{\rm inst}(\tau)$.

of the free energy at $u = \pm u_0$ (see Appendix B). The solution of the instanton trajectory $u_{\rm inst}(\tau)$ can be defined implicitly via

$$\tau = \int_{-u_0}^{u_{\rm inst}(\tau)} \frac{du}{\sqrt{2\omega_0[\mathcal{F}_{\rm DI}(u) - \mathcal{F}_{\rm DI}(-u_0)]}}. \tag{24}$$

We find that in the superradiant phase, the instanton trajectory always crosses two special points $u = \pm J/g$ [see Fig. 2(f)]. According to Eq. (22) for the magnon spectrum, the Ising chain becomes critical due to the gap closing at these points. This crossing occurs because $u_{\rm inst}$ has support in the interval $[-u_0; u_0]$, which includes these special points since $|J/g| < u_0$, as implied by Eq. (21). We conclude that the fluctuations above the QPT are nonvanishing; in other words, the system remains critical in the superradiant phase. This behavior contrasts with the conventional Dicke model, which is critical only at the transition point. We can also draw an imaginary-time analogy of the Kibble-Zurek mechanism around the second-order Ising QPT. In our case, the Ising transition is virtual and hidden in the superradiant phase.

E. Angular representation at $\omega_z \neq 0$ and $s \geqslant \frac{1}{2}$

As mentioned above, the presence of special points on the instanton trajectory indicates critical fluctuations at $\omega_z = 0$ in this model, attributed to the gapless spectrum. However, the gap reemerges at finite ω_z. The analytic derivation of $\mathcal{F}_{\rm DI}$ for this general case of $\omega_z \neq 0$ is more involved: Neither the Jordan-Wigner nor the Majorana representation of the Pauli operators yields a quadratic action over fermions. Therefore, the exact Gaussian integration over spin states used in the derivations of Eqs. (20) and (21) does not apply.

An alternative representation of spins with arbitrary s is provided by [sketch shown in Fig. 3(a)]

$$\begin{aligned} \hat{\sigma}_j^x &\to 2s \sin\vartheta_j \sin\phi_j, \\ \hat{\sigma}_j^y &\to 2s \cos\vartheta_j, \\ \hat{\sigma}_j^z &\to 2s \sin\vartheta_j \cos\phi_j. \end{aligned} \tag{25}$$

As the number of excited states is $2s$, qubits correspond to $s = \frac{1}{2}$, *qutrits* to $s = 1$, and so on. In the path integral for the partition function, ϑ_j and ϕ_j are real bosonic fields,

$$Z = \int d[\{\phi, \vartheta\}_j^N, u] \exp(-S[\{\phi, \vartheta\}_j^N, u]), \tag{26}$$

and the full Matsubara action reads as

$$S = S_{\rm WZNW} + \int_0^{1/T} d\tau\, (\bar{a}\partial_\tau a + H_{\rm DI}). \tag{27}$$

This is the sum of the Wess-Zumino-Novikov-Witten action

$$S_{\rm WZNW} = -is \sum_j \int_0^{1/T} d\tau\, \dot{\phi}_j (1 - \cos\vartheta_j), \tag{28}$$

i.e., the integral over the spin Berry phase, the kinetic term for the photon field $\sim \bar{a}\partial_\tau a$, and finally the Dicke-Ising Hamiltonian parametrized by Eq. (25).

In the limit of small photon frequency $\omega_0 \ll J,\ g$ and finite ω_z, a mean-field solution can be found as this regime of energy scales allows one to consider $u(\tau)$ as a *slow* variable. The trajectories contributing to Z then effectively reside near the xz plane, with small, rapid out-of-plane fluctuations, i.e.,

$$\vartheta_j(\tau) = \frac{\pi}{2} + \Delta\vartheta_j(\tau). \tag{29}$$

The corresponding geometric interpretation is shown in Fig. 3(a). The logic of separation into slow and fast components is also applicable to the in-plane components

$$\phi_j(\tau) = \phi(\tau) + \Delta\phi_j(\tau), \tag{30}$$

with a slow collective angle $\phi(\tau)$ and rapid fluctuations $\Delta\phi_j(\tau)$.

F. Quasiclassical approach for fluctuations

Further progress can be achieved in the quasiclassical limit where one assumes that the fluctuations near the mean-field trajectory are small. We start from the mean-field solution for free energy, neglecting all angle fluctuations, i.e., $\Delta\vartheta_j(\tau) = \Delta\phi_j(\tau) = 0$. We also assume that ω_0 is smaller than other energy scales, which guarantees that $u(\tau)$ and $\phi(\tau)$ are slow. The resulting mean-field action reads as

$$S_{\rm mf} = N \int_0^\infty d\tau \left(\frac{(\partial_\tau u)^2}{4\omega_0} + \mathcal{F}_{\rm mf}(u, \phi) \right), \tag{31}$$

where the mean-field free energy is

$$\mathcal{F}_{\rm mf}(u, \phi) = \tfrac{1}{4}\omega_0 u^2 + h(u, \phi). \tag{32}$$

Here, $h(u, \phi)$ corresponds to the spin part of the Hamiltonian with homogeneous configurations of $\phi_j = \phi$ and $\vartheta_j = \pi/2$,

$$h(u, \phi) = 2s(-\omega_z \cos\phi + gu \sin\phi - 2sJ \cos^2\phi). \tag{33}$$

The profile of (33) in the superradiant phase is shown in Fig. 3(b), where the two minima correspond to the distinct macroscopic superradiant states $|\Psi_R\rangle$ and $|\Psi_L\rangle$. As long as there is no time-derivative term for ϕ in $S_{\rm mf}$, nontrivial contributions to Z are given only by the single quantum trajectory $\tilde{\phi}(u_{\rm inst})$ that connects these two minima, i.e.,

$$Z \sim e^{-S_{\rm mf}[u_{\rm inst}(\tau)]}. \tag{34}$$

The value of Z then determines the amplitude of macroscopic quantum tunneling.

The angular dependence $\tilde{\phi}(u)$ is determined by the condition $\partial_\phi \mathcal{F}_{\rm mf}(u,\phi)=0$. The motion of $u(\tau)$ along the quantum trajectory is described by a modified instanton equation

$$\frac{\ddot{u}}{2\omega_0}+\partial_u \mathcal{F}_{\rm mf}(u,\tilde{\phi}(u))=0 \tag{35}$$

with boundary conditions $u(0)=-u(1/T)=-u_0$. Again, a sketch of the instanton solution is shown in Fig. 3(c).

The next step of our quasiclassical approach is to calculate the quantum corrections $\mathcal{F}_{\rm fl}$ to the mean-field potential $\mathcal{F}_{\rm mf}$ caused by the Gaussian fluctuations of $\Delta\vartheta_j(\tau)$ and $\Delta\phi_j(\tau)$ neglected previously. To this end, we expand S given by (27) to second order in $\Delta\vartheta_j(\tau)$ and $\Delta\phi_j(\tau)$:

$$S=S_{\rm mf}[u,\phi]+S_{\rm G}[u,\phi,\Delta\vartheta,\Delta\phi]. \tag{36}$$

This is a sum of the mean-field action (33) and the Gaussian part $S_{\rm G}$ given by

$$S_{\rm G}=\frac{1}{2}\int_0^{1/T}d\tau\int_{-\pi}^{\pi}\frac{d\mathbf{k}}{2\pi}[\Delta\vartheta \quad \Delta\phi]_{-\mathbf{k}} \times\begin{bmatrix}\mathcal{A}(u,\phi) & -is\partial_\tau\\ is\partial_\tau & \mathcal{B}_{\mathbf{k}}(u,\phi)\end{bmatrix}\begin{bmatrix}\Delta\vartheta\\ \Delta\phi\end{bmatrix}_{\mathbf{k}}, \tag{37}$$

where the matrix elements depend on the slow trajectories. Note that the action does not have a linear contribution because we assume that $\sum_j\Delta\vartheta_j=\sum_j\Delta\phi_j=0$. For the term $\sim\Delta\vartheta^2$, the element $\mathcal{A}$ partially coincides with h from (32),

$$\mathcal{A}(u,\phi)=4Js^2\cos^2\phi-h(u,\phi). \tag{38}$$

The amplitude of the term $\sim\Delta\phi^2$ involves the momentum dependence

$$\mathcal{B}_{\mathbf{k}}(u,\phi)=\mathcal{A}(u,\phi)-8Js^2\sin^2\phi\cos\mathbf{k}. \tag{39}$$

The stability of the action (37) along the trajectory $\tilde{\phi}(u)$ is provided by the joint condition $\mathcal{A}(u,\phi)>0$ and $\mathcal{B}_{\mathbf{k}}(u,\phi)>0$ for all $\mathbf{k}$. It is equivalent to

$$4sJ\cos 2\phi+\omega_z\cos\phi-gu\sin\phi>0. \tag{40}$$

Assuming that (40) is satisfied and u and ϕ are slow (adiabatic limit), the Gaussian integration over the fields $\Delta\vartheta_{\mathbf{k}}$ and $\Delta\phi_{\mathbf{k}}$ yields the fluctuation correction $S_{\rm fl}[u,\phi]$ to the mean-field action. This correction reads as

$$S_{\rm fl}=N\int_{-\pi}^{\pi}\frac{d\mathbf{k}}{2\pi}\ln\prod_{n\geqslant 1}\left(1+\frac{\mathcal{A}(u,\phi)\mathcal{B}_{\mathbf{k}}(u,\phi)}{(2\pi sTn)^2}\right). \tag{41}$$

We calculate the infinite product over the Matsubara index $n\geqslant 1$ using the identity (A12) from the Appendix. After that, we take the limit $T\to 0$ in the definition for the free-energy correction $\mathcal{F}_{\rm fl}=N^{-1}TS_{\rm fl}$ and find

$$\mathcal{F}_{\rm fl}(u,\phi)=\frac{1}{2s}\int_{-\pi}^{\pi}\frac{d\mathbf{k}}{2\pi}\sqrt{\mathcal{A}(u,\phi)\mathcal{B}_{\mathbf{k}}(u,\phi)}. \tag{42}$$

The integral over $\mathbf{k}$ yields

$$\mathcal{F}_{\rm fl}(u,\phi)=\frac{1}{\pi s}\sqrt{\mathcal{A}(u,\phi)(\mathcal{A}(u,\phi)+8s^2J\sin^2\phi)} \times\mathrm{E}\left(\frac{16s^2J\sin^2\phi}{\mathcal{A}(u,\phi)+8s^2J\sin^2\phi}\right). \tag{43}$$

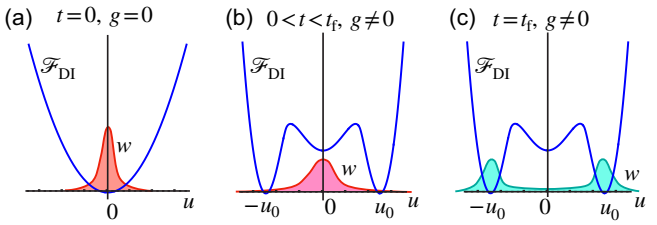

FIG. 4. Sketch illustrating the quench dynamics of the photon probability distribution $w(x,t)$ in the potential formed by the free energy $\mathcal{F}_{\rm DI}(u)$. (a) Gaussian $w(x,t)$ at $t=0$ when $g=0$. (b) Evolution of $w(x,t)$ after the quench of g from 0 to $g\approx g_c$. (c) End of the evolution at $t=t_{\rm f}$ shows two maxima of $w(x,t_{\rm f})$ at $u=\pm u_0$ corresponding to superradiant condensates.

In the Dicke-model limit $J=0$, we use $\mathcal{A}=-h$ and obtain

$$\mathcal{F}_{\rm fl}=-\frac{1}{2s}h(u,\phi). \tag{44}$$

The full free energy then reads as

$$\mathcal{F}_{\rm mf}+\mathcal{F}_{\rm fl}=\frac{1}{4}\omega_0u^2+\left(1-\frac{1}{2s}\right)h(u,\phi). \tag{45}$$

One can see from (45) that the fluctuation correction is small at $s\gg 1$. The Dicke model for large spins has been studied recently in Ref. [57] where the authors predicted multicritical behavior at QPT. For nonzero J, one also finds $\mathcal{F}_{\rm fl}/\mathcal{F}_{\rm mf}\sim s^{-1}$. Therefore, in the large-spin limit, the fluctuations are small and the quasiclassical approach is legitimate.

In the following, based on our understanding of the free-energy profile $\mathcal{F}$, we formulate a quench protocol for the simulation of the condensate dynamics.

IV. HYBRID QUANTUM CIRCUIT

A. Approximation of the superradiant ground state via quench

Our remaining objective is to obtain an approximate superradiant state from a finite quantum circuit, which takes the form of unitary evolution on the time interval $t\in[0;t_{\rm f}]$ starting from the trivial ferromagnetic state for spin $s=\frac{1}{2}$, $|\mathrm{FM}\rangle$. Note that $|\mathrm{FM}\rangle$ is an eigenstate of $\hat{H}_{\rm DI}$ at $g=0$. The final state $|\Psi(t)\rangle=e^{-i\hat{H}_{\rm DI}t}|\mathrm{FM}\rangle$ is supposed to be close to the exact eigenstate $|\mathrm{SR}\rangle$. The evolution with $\hat{H}_{\rm DI}$ can be understood as a quench after the coupling g is switched on at $t=0$.

In coordinate representation, the photon distribution at $t=0$ is a Gaussian wave packet, i.e.,

$$w(u,t=0)=\frac{1}{\sqrt{\pi}}e^{-u^2N}, \tag{46}$$

which can be interpreted as an eigenstate of a particle in the parabolic free-energy profile $\mathcal{F}_{\rm DI}(u)$ at $g=0$ [see Fig. 4(a)]. We note that, when sending $N\to\infty$, the wave packet $w(u,t)$ tends to a δ singularity, which is the classical limit.

As sketched in Fig. 4(b), the quench induces an instantaneous change to $\mathcal{F}_{\rm DI}(u)$, and the Gaussian packet tunnels into the side minima; the evolution should stop at the moment $t=t_{\rm f}$ when $w(u,t_{\rm f})$ is concentrated in either of these minima [Fig. 4(c)]. The many-body wave function $|\Psi(t)\rangle$ then

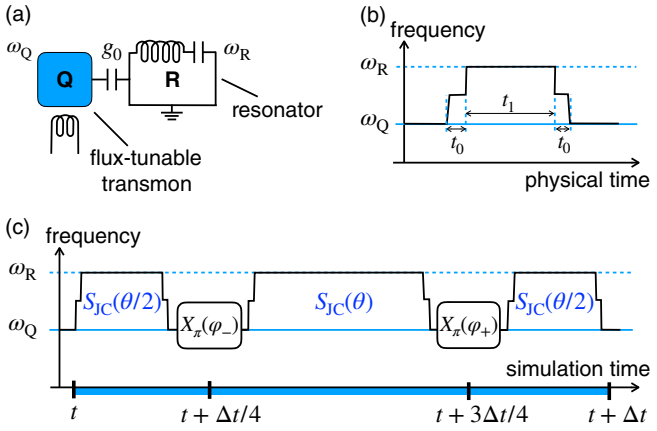

FIG. 5. (a) Qubit-resonator architecture for the Rabi model. (b) Resonant pulse for the Jaynes-Cummings gate. (c) Pulse sequence representing the Rabi gate.

contains a substantial amount of condensed photons, which is used in the further protocol detailed below.

B. Rabi, Jaynes-Cummings, and Dicke gates

We take inspiration from the digital-analog approach of Refs. [43,44], where the authors suggested to simulate the quantum Rabi model

$$\hat{H}_R = \omega_0 \hat{a}^\dagger \hat{a} + g(\hat{a} + \hat{a}^\dagger)\hat{\sigma}^x \tag{47}$$

through a combination of single-qubit rotations and a hybrid Jaynes-Cummings (JC) gate

$$\hat{S}_{JC}(\theta) = \exp[-i\theta(\hat{a}^\dagger \hat{\sigma}^- + \hat{a}\hat{\sigma}^+)], \tag{48}$$

where $\hat{\sigma}^\pm = \frac{1}{2}(\hat{\sigma}^x \mp i\hat{\sigma}^y)$. The JC gate enables efficient rotations in the joint qubit-resonator Hilbert space. We have in mind an architecture as shown in Fig. 5(a), where a tunable transmon qubit (Q) with physical frequency ω_Q is coupled to a superconducting resonator (R), modeled as an LC circuit with fundamental frequency ω_R. The JC gate can be implemented as a flux pulse applied to Q, similar to two-qubit XY gates [58]. A sketch of the pulse envelope is shown in Fig. 5(b). The pulse tunes ω_Q into a resonance with ω_R during the *physical* time t_1, which enables the system to acquire the desired relative phase $\theta = g\Delta t = g_0 t_1$ where Δt is the Trotterization time *in the simulation*, and g_0 is the *physical* qubit-resonator coupling. The additional buffer steps t_0 may be used to gauge out dynamic phases in $\hat{S}_{JC}$.

Reproducing the logic of Ref. [44], we now derive the Rabi gate from the JC gate and then generalize the former to a Dicke gate. The original idea is to decompose Eq. (47) into

$$\hat{H}_R = \tfrac{1}{2}(\hat{H}_{JC} + \hat{H}_{AJC}) \tag{49}$$

where

$$\hat{H}_{JC} = \hat{H}_0 + 2g(\hat{a}^\dagger \hat{\sigma}^- + \hat{a}\hat{\sigma}^+) \tag{50}$$

is the Jaynes-Cummings Hamiltonian and

$$\hat{H}_{AJC} = \hat{\sigma}^x \hat{H}_{JC} \hat{\sigma}^x \tag{51}$$

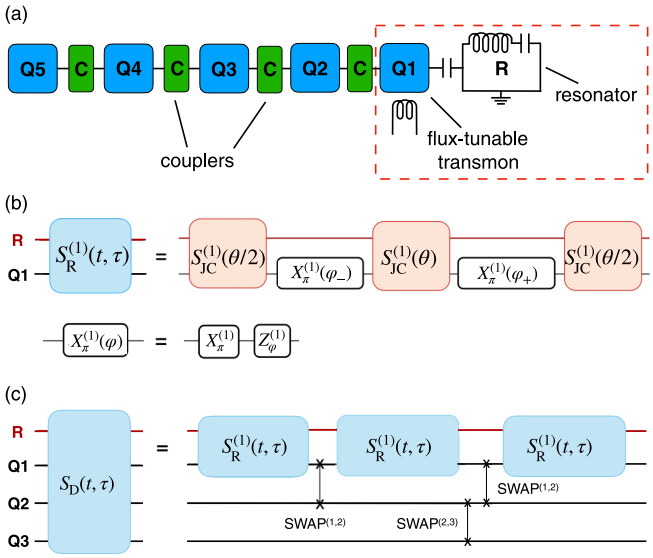

FIG. 6. (a) Qubit-boson architecture for the Dicke-Ising model. Dashed red box: Rabi gate block for the first qubit. Also shown are quantum circuits representing (b) the Rabi and (c) Dicke gates. The gate $X_\pi^{(1)}(\varphi)$ is acting to the first qubit.

is the corresponding counter-rotating interaction term. The free part can be chosen as

$$\hat{H}_0 = \omega_0(\hat{a}^\dagger \hat{a} - \hat{\sigma}^z/2). \tag{52}$$

The exact Trotter step $e^{-i\hat{H}_R \Delta t}$ on the simulation time interval $[t; t+\Delta t]$ is approximated to second order by

$$\hat{U}_R(t+\Delta t, t) = e^{-i\hat{H}_{JC}\Delta t/4} e^{-i\hat{H}_{AJC}\Delta t/2} e^{-i\hat{H}_{JC}\Delta t/4}, \tag{53}$$

which has a discretization error of $O(\Delta t^3)$. Moving to the frame rotating with $\hat{H}_0$, one obtains

$$\hat{U}_R(t+\Delta t, t) = e^{-i\hat{H}_0(t+\Delta t)} \hat{S}_R(t+\Delta t, t) e^{i\hat{H}_0 t} \tag{54}$$

where $\hat{S}_R$ is the hybrid qubit-resonator gate sequence

$$\hat{S}_R = \hat{S}_{JC}(\theta/2)\hat{X}_\pi(\varphi_+)\hat{S}_{JC}(\theta)\hat{X}_\pi(\varphi_-)\hat{S}_{JC}(\theta/2), \tag{55}$$

where the phases are $\varphi_- = \omega_0(t + \Delta t/4)$ and $\varphi_+ = \omega_0(t + 3\Delta t/4)$. For explicit derivation of the latter equation, see Appendix C. This gate has been realized experimentally as a pulse sequence [44], which is shown schematically in Fig. 5(c). It consists of three analog JC gates separated by single-qubit gates, which we have combined in the definition

$$\hat{X}_\pi(\varphi_\pm) = \exp(-i\varphi_\pm \hat{\sigma}^z)\hat{\sigma}^x. \tag{56}$$

These single-qubit gates encode the counter-rotating evolution due to $\hat{H}_{AJC}$ as well as the necessary rotating-frame transformations.

With the multiqubit architecture of Fig. 6(a) in mind, where only one qubit is *physically* coupled to the resonator, we propose a Dicke gate $\hat{S}_D$ implemented by applying the Rabi gate Fig. 6(b) to Q1 only, while digital SWAP gates mediate the interaction to the other qubits Q2 and Q3 [Fig. 6(c)]. An alternative architecture analogous to the experimental setting of Ref. [47] is suggested in Fig. 7. Compared to Fig. 6(a), all qubits are tunable and directly coupled to the resonator via the

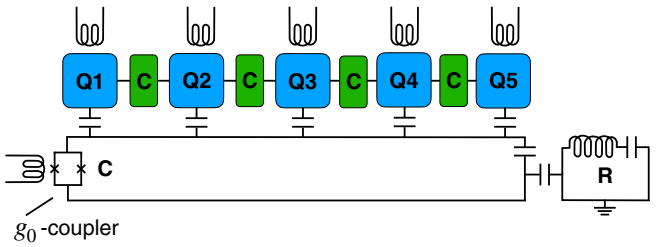

FIG. 7. Alternative qubit-boson architecture with all qubits tunable and coupled to the resonator. The auxiliary qubit acts as a coupler (C) to the resonator with tunable g_0.

additional g_0 coupler. Rabi gates can then be applied to each of the qubits without the need for additional SWAP gates.

C. Algorithm overview

The full algorithm, which starts from $|\mathrm{FM}\rangle$, is shown in Fig. 8. In each Trotter step, the Dicke gate $\hat{S}_\mathrm{D}$ is followed by a set of single-qubit Z gates and two-qubit ZZ gates, which simulate the onsite frequencies ω_z and the Ising interactions in Eq. (1) via

$$ZZ_{\eta,j} = e^{i\eta\hat{\sigma}^z_j\hat{\sigma}^z_{j+1}},\ Z_{\beta,j} = e^{i\beta\hat{\sigma}^z_j}, \tag{57}$$

where the phases are given by $\eta = J\Delta t$ and $\beta = \omega_z\Delta t$. Together, these gates constitute our Dicke-Ising gate $\hat{S}_\mathrm{DI}$, which governs the Trotterized evolution under the Hamiltonian $\hat{H}_\mathrm{DI}$ in the photon-coupled interaction picture:

$$\hat{U}_0^\dagger(t)e^{-i\hat{H}_\mathrm{DI}t} \approx \prod_{k=1}^{L}\hat{S}_\mathrm{DI}(t_k,\Delta t). \tag{58}$$

Here $\hat{U}_0(t) = e^{-iH_0t}$ is the free unitary evolution with the Hamiltonian

$$\hat{H}_0 = \omega_0\hat{a}^\dagger\hat{a} - \frac{1}{2}\omega_0\sum_{j=1}^{N}\hat{\sigma}^z_j, \tag{59}$$

which form is chosen similar to Eq. (52) used previously. The Trotter step index k runs from 1 to L, with the simulation times given by $t_k = (k-1)\Delta t$ and the Trotter step size $\Delta t = t/L$.

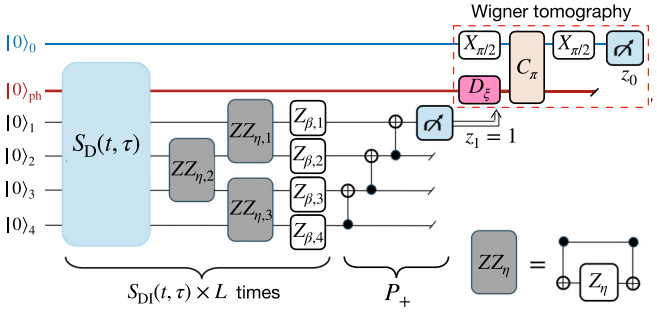

FIG. 8. Full quantum circuit implementing the cat state and Wigner tomography. The circuit with L Trotter steps and N qubits requires $3LN$ JC gates and $(2L+1)(N-1)$ two-qubit CNOT gates. Assuming the architecture shown in Fig. 6(a), the algorithm involves $\frac{1}{2}LN(N-1)$ SWAPs. The alternative architecture from Fig. 7 does not require SWAPs.

The Dicke-Ising gate appearing in (58) is constructed as

$$\hat{S}_\mathrm{DI}(t_k,\Delta t) = \left(\prod_{j=1}^{N-1}ZZ_{\eta,j}\right)\left(\prod_{j=1}^{N}Z_{\beta,j}\right)\hat{S}_\mathrm{D}(t_k,\Delta t). \tag{60}$$

Depending on the architecture shown either in Fig. 6(a) or in 7, the Dicke gate $\hat{S}_\mathrm{D}$ in (60) takes the form

$$\hat{S}_\mathrm{D} = \begin{cases} \hat{S}^{(1)}_\mathrm{R}\prod_{j=1}^{N-1}\left(\left(\prod_{l=1}^{j}\mathrm{SWAP}^{(j-l+1,j-l+2)}\right)\hat{S}^{(1)}_\mathrm{R}\right), & \text{[Fig. 6(a)]};\\ \prod_{j=1}^{N}\hat{S}^{(j)}_\mathrm{R}, & \text{[Fig. 7]}. \end{cases} \tag{61}$$

The Rabi gates $\hat{S}^{(j)}_\mathrm{R}$ are defined in Eq. (55). The associated phases are given by $\varphi_+(t_k) = \omega_0(t_k + 3\Delta t/4)$, $\varphi_-(t_k) = \omega_0(t_k + \Delta t/4)$, and the coupling angle is $\theta = \frac{g\Delta t}{\sqrt{N}}$. A full derivation of the decomposition in Eqs. (58)–(61) is provided in Appendix C.

At the end of the full Trotter evolution, we arrive at the many-body state $|\Psi(t_\mathrm{f})\rangle \approx |\mathrm{SR}\rangle$ that approximates the exact superradiant state. The Trotter evolution is followed by a controlled NOT (CNOT) sequence (emulating $\hat{P}_+$) and measurement of the first qubit. As proposed in [59], this CNOT sequence yields the parity by measuring only a single qubit instead of all of them. If the measurement result is $z_1 = 1$, then one performs Wigner tomography of the resonator. If $z_1 = -1$, the tomography is not performed. This completes our algorithm. The Wigner tomography circuit is shown in Fig. 8 inside the dashed contour. We follow the ideas of the measurement protocols suggested in Refs. [44,54,60]. There is a representation of the Wigner function equivalent to Eq. (10) that reads as

$$W_\xi = \frac{2}{\pi}\mathrm{tr}(\hat{\Pi}\hat{D}^\dagger_\xi\hat{\rho}_\mathrm{ph}\hat{D}_\xi), \tag{62}$$

where the photon-state density matrix ρ_ph is given by the projection of the full many-body state on a certain spin configuration. Here, $\hat{\Pi} = e^{i\pi\hat{a}^\dagger\hat{a}}$ is the photon parity operator, $\hat{D}_\xi = e^{\xi\hat{a}^\dagger - \xi^*\hat{a}}$ is the standard displacement operator with the complex phase $\xi = x + ip$ parametrized by x and p. The displacement operator can be implemented as a drive pulse applied to the resonator. It is depicted as the gate D_ξ in Fig. 8. The density matrix $\hat{\rho}_\mathrm{ph}$ becomes $\hat{D}^\dagger_\xi\hat{\rho}_\mathrm{ph}\hat{D}_\xi$ after this pulse. The parity operator $\hat{\Pi}$ is implemented (i) via the gate C_π entangling the resonator with an off-resonant ancilla qubit and (ii) via two $X_{\pi/2}$ gates to perform Ramsey interferometry. Measuring the ancilla in the computational basis yields the photon parity $\Pi = \pm 1$ via the measurement value z_0. The measurement is performed repeatedly to obtain the respective probabilities $\mathcal{P}(z_0 = \pm 1)$, the difference of which yields the Wigner function value W_ξ. To implement this protocol on a physical level, we have in mind the standard dispersive Hamiltonian for the resonator and the ancilla qubit with frequency $\omega^{(0)}_\mathrm{Q}$,

$$\hat{H}_\mathrm{disp} = \omega_\mathrm{R}\hat{a}^\dagger\hat{a} + \omega^{(0)}_\mathrm{Q}|1\rangle\langle 1| - \chi\hat{a}^\dagger\hat{a}|1\rangle\langle 1|. \tag{63}$$

The evolution with $\hat{H}_\mathrm{disp}$ during time interval δt yields the operator $\hat{U}_\Phi = |0\rangle\langle 0| + e^{i\Phi\hat{a}^\dagger\hat{a}}|1\rangle\langle 1|$ with phase $\Phi = \chi\delta t$.

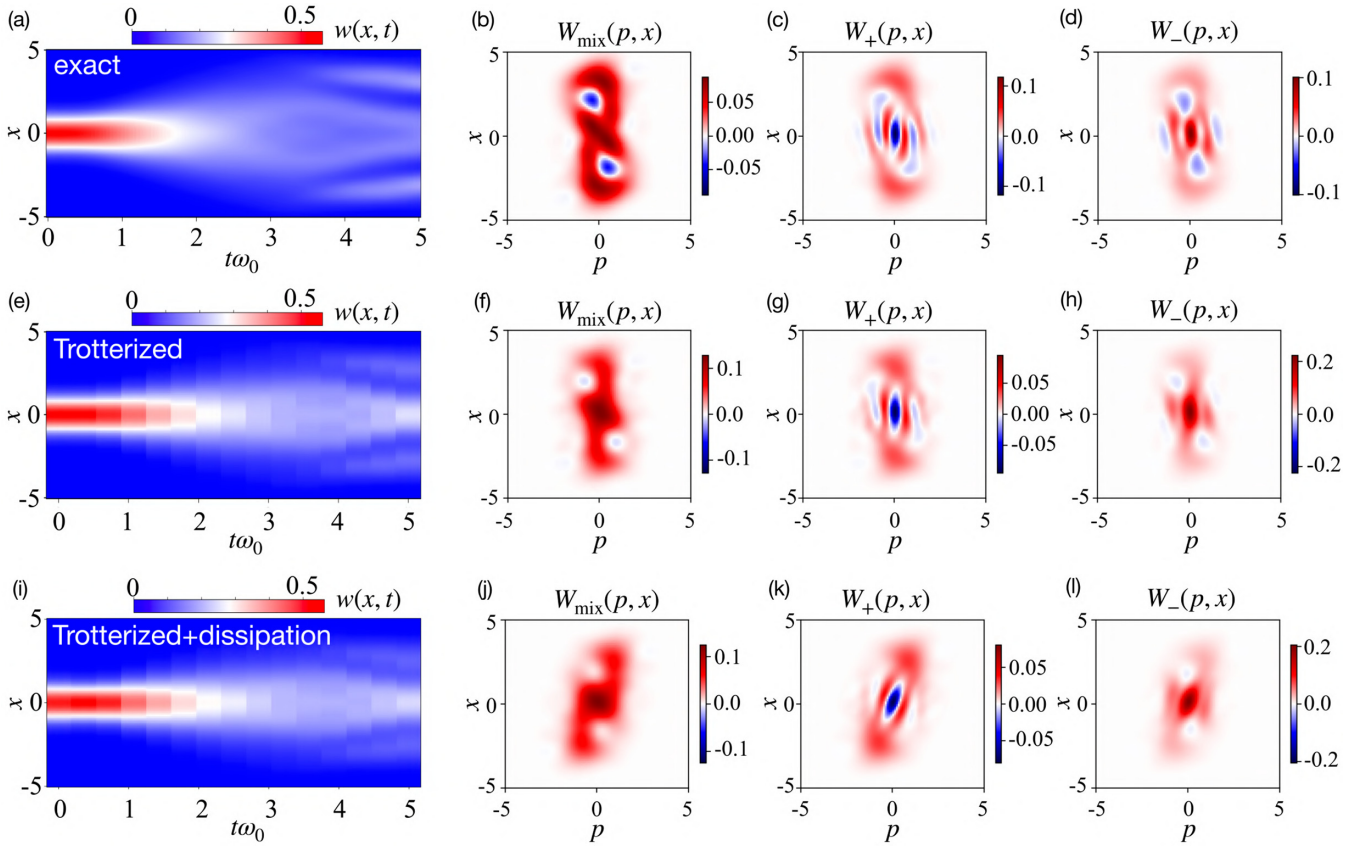

FIG. 9. Numerical simulations of exact and Trotter evolutions, without and with dissipation. (a) Exact dynamics of the photon probability distribution $w(x,t)$ after the quench during time $t \in [0,\ t_{\rm f}]$. Wigner functions at the end of evolution $t = t_{\rm f}$: (b) $W_{\rm mix}$ without parity selection, (c) W_+ for the positive parity, which shows cat-state signatures, and (d) W_- for the negative parity sector. (e)–(h) The data for $w(x,t)$, $W_{\rm mix}$, and $W_\pm$ emulated by means of our quantum algorithm as depicted in Fig. 8 with $L = 15$ Trotter steps. The parameters are $N = 5$ qubits, a Fock-space cutoff at 20 photons, $\omega_z/\omega_0 = 0.05$, $J/\omega_0 = 1$, and $g/\omega_0 = 0.9$, which places the system slightly above the QPT. (i)–(l) Data for emulation with a Lindbladian dissipation (D1) added after each of the Dicke-Ising gates. The *physical* duration time of each constituent Rabi gate is assumed to be $\tau_{\rm Rabi} = 100$ ns; the decay rates are $\kappa = 2\pi \times 1$ kHz for the resonator and $\Gamma_\phi = \Gamma_1 = 2\pi \times 5$ kHz for the qubits.

Before the tomography, the ancilla qubit is in the state $|\psi_0\rangle = |0\rangle$; the $X_{\pi/2}$ gate brings it into the superposition $|\psi_1\rangle = \frac{1}{\sqrt{2}}(|0\rangle + i|1\rangle)$. After that, by tuning the duration δt of the off-resonant evolution such that $\Phi = \pi$, the entangling gate C_π can be realized. Depending on the photon parity, C_π rotates the qubit state either over the angle π or 2π along the Bloch-sphere equator. The ancilla wave function then becomes $|\psi_2\rangle = \frac{1}{\sqrt{2}}(|0\rangle + i\Pi|1\rangle)$. The second $X_{\pi/2}$ gate and subsequent z_0 measurement finalize the Ramsey interferometry. As a result, one measures the state $|\psi_3\rangle = |1\rangle$ if the parity is even ($\Pi = 1$) or $|\psi_3\rangle = |0\rangle$ if the parity is odd ($\Pi = -1$).

V. DISCUSSION

Illustrative results of our numerical simulations of the Dicke-Ising Hamiltonian with $N = 5$ qubits are shown in Fig. 9. Our data include temporal evolution of the photon probability distribution $w(x,t)$ as well as the Wigner functions $W_{\rm mix}$, W_+ at the very end of the time evolution. In Fig. 9(a) we show the exact dynamics of $w(x,t)$ when the evolution starts with a Gaussian distribution $w(x,0) = e^{-x^2}/\sqrt{\pi}$, which corresponds the many-body wave function $|\Psi(t{=}0)\rangle = |{\rm FM}\rangle$. At the end of the evolution ($\omega_0 t_{\rm f} = 5$), the wave function $|\Psi_{t_{\rm f}}\rangle$ is supposed to be similar to $|{\rm SR}\rangle$. The distribution $w(x,t_{\rm f})$ indeed has well-defined side peaks around $x \approx \pm 4$, which correspond to a finite amount of condensed photons.

While the Wigner functions $W_{\rm mix}$ and W_+ at $t = t_{\rm f}$ [Figs. 9(b) and 9(c)] look distorted, they are qualitatively similar to the ideal distributions shown in Figs. 1(c) and 1(d). It is important to note that W_+ in Fig. 9(c) retains clear cat-state signatures, visible as blue stripes of negative quasiprobabilities. In Figs. 9(e) and 9(h), we present the equivalent simulation of the Trotterized dynamics with 15 steps according to our digital-analog algorithm given in Fig. 8. The Wigner functions found through the Trotter evolution [Figs. 9(f) and 9(g)] are in good agreement with the exact simulation results in Figs. 9(b) and 9(c), respectively. The Wigner functions W_- [Figs. 9(d) and 9(h)] also exhibit negative values, although these are less pronounced than in W_+.

In Figs. 9(i)–9(l), we show simulation data for Trotterized evolution in the presence of noise in the circuit, which is modeled by the Lindbladian dynamics of the density matrix; details are provided in Appendix D. This model simulates dissipative processes of individual qubits and photons during

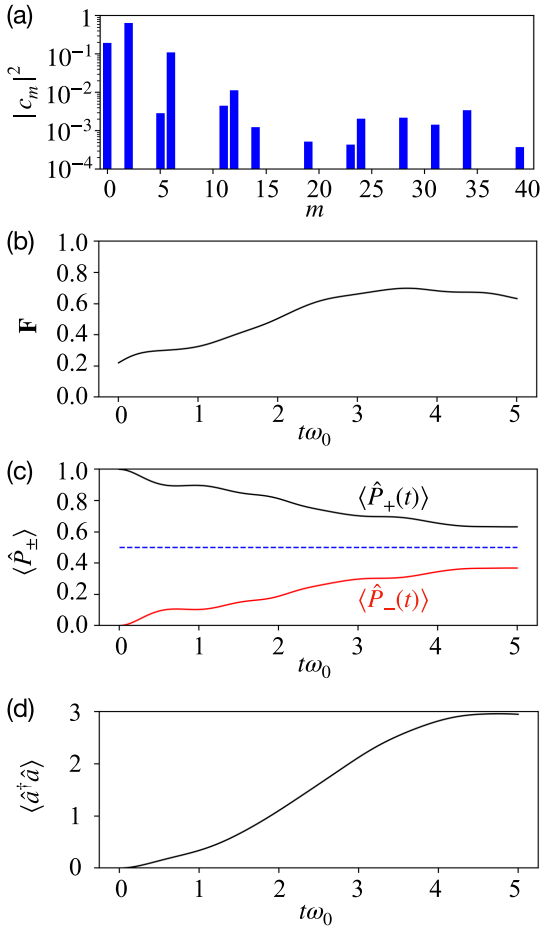

FIG. 10. (a) Expansion coefficients $|c_m|^2$ of the *ferromagnetic* initial state over the eigenbasis of $\hat{H}_{\rm DI}$. (b)–(d) Results for the exact time evolution after the quench, with Hamiltonian parameters identical to those used in Fig. 9. (b) Fidelity $\mathbf{F}(t)$ between the reduced density matrices for photons corresponding to the simulated wave function $\rho(t)$ and the ground state of $\hat{H}_{\rm DI}$, $\rho_{\rm SR}$. (c) Time dependence of the probabilities to measure positive and negative qubit parities $\langle \hat{P}_\pm(t) \rangle$. (d) Time dependence of the photon number $\langle \hat{a}^\dagger \hat{a} \rangle$.

the *physical* operation time of Rabi gates. In our simulations, we choose eperimentally relevant qubit decay rates of $\Gamma_\phi = \Gamma_1 = 2\pi \times 5$ kHz [47] and Rabi gate time of $\tau_{\rm Rabi} = 100$ ns [44]. As the simulations show, the signatures of cat states are well resolved for high-quality resonators with decay rates κ of just a few kiloherz [49].

Under exact quench dynamics, the many-body wave function $|\Psi(t)\rangle$ evolves as a superposition of the eigenstates $|\Psi_m\rangle$ of the Hamiltonian $\hat{H}_{\rm DI}$:

$$|\Psi(t)\rangle = \sum_m e^{-i\varepsilon_m t} c_m |\Psi_m\rangle. \tag{64}$$

Here, m enumerates all many-body eigenstates, with $m = 0$ corresponding to the ground state and $m \geqslant 1$ to the excited states. The expansion coefficients $c_m = \langle \Psi_m | {\rm FM} \rangle$ are the overlaps of the eigenstates with the initial *ferromagnetic* state $|{\rm FM}\rangle$. In Fig. 10(a), we show the squared overlap coefficients $|c_m|^2$ for $0 \leqslant m \leqslant 40$. The nonvanishing overlap between the *ferromagnetic* initial state and the exact superradiant ground state $|{\rm SR}\rangle = |\Psi_0\rangle$ is given by $|c_0|^2 \approx 0.2$, which reflects the small underbarrier tunnel probability in the ground state slightly above the critical point.

In Figs. 10(b)–10(d) we show results for the exact time evolution after the quench. Figure 10(b) shows the temporal dependence of the fidelity $\mathbf{F}(t) = (\mathrm{tr}\sqrt{\sqrt{\rho_{\rm SR}}\rho(t)\sqrt{\rho_{\rm SR}}})^2$ between the reduced density matrices $\rho(t) = \mathrm{tr}_\sigma[|\Psi(t)\rangle\langle\Psi(t)|]$ and $\rho_{\rm SR} = \mathrm{tr}_\sigma[|{\rm SR}\rangle\langle{\rm SR}|]$. The nonzero overlap and fidelity indicate that more than half of the total photon population resides in the superradiant condensate. Also in Fig. 10(c) , we present the time evolution of the probabilities to measure even or odd qubit parity, $\langle \hat{P}_\pm(t) \rangle$. These begin at $\langle \hat{P}_+ \rangle = 1$ and $\langle \hat{P}_- \rangle = 0$ at $t = 0$, reflecting fully imbalanced initial probabilities, and approach $\frac{1}{2}$ at the final time $t = t_{\rm f}$. This parity equalization provides an additional signature of superradiance in this protocol.

In Fig. 10(d) we show the time dependence of the photon number $\langle \hat{a}^\dagger \hat{a} \rangle$ after the quench. It starts from zero in the normal phase and increases to ≈ 3 at the final time, confirming that boundary effects from the 20-photon Fock-space cutoff are negligible.

For the total gate count, we obtain the following estimation. Each Rabi gate $S_{\rm R}$ involves three JC gates. Assuming the 1D qubit-boson architecture from Fig. 6(a), where the qubit at one end of the chain is coupled to the resonator, the Dicke gate $S_{\rm D}$ has N $S_{\rm R}$ gates and $\frac{1}{2}N(N-1)$ SWAPs. For the star-chain hybrid geometry from Fig. 7, SWAPs are not required. The Dicke-Ising $S_{\rm DI}$ gate has one $S_{\rm D}$ gate and $2(N-1)$ CNOTs. Parity selection involves $(N-1)$ CNOTs. To summarize, the circuit with L Trotter steps requires

$$\begin{cases} \frac{1}{2}LN(N-1) & \text{[1D chain Fig. 6(a)]} \\ 0 & \text{[star-chain Fig. 7]} \end{cases} \quad \text{SWAPs},$$

$(2L+1)(N-1)$ CNOTs,

$3LN$ JC gates.

Based on these numbers, we conjecture that the algorithm is capable of simulating the QPT after a quench as well as the cat-state preparation with a finite depth quantum circuit without fine-tuning parameters.

The Wigner tomography represents a substantial experimental overhead. It requires careful calibration of the dispersive coupling strength (χ) and evolution time (δt). To achieve an adequate resolution in the phase space, a two-dimensional grid of displacement complex parameter ξ must be sampled, typically to $\sim 10^2 \times 10^2$ points [54]. At each point, repeated ancilla qubit measurements (on the order of 10^3 shots) are necessary to accurately estimate the parity expectation value, resulting in total counts around several million. Ideally, the dispersive interaction enables quantum nondemolition measurements of the photon parity. In practice, the readout process introduces partial backaction on the resonator's state. The qubit measurement does not fully collapse the resonator into a specific Fock state, but rather into a state with a given parity that preserves some coherence within the corresponding Hilbert subspace.

While implementing the continuous-variable representation with x and p, one concerns about resonator's leakage. In

the superconducting platform, the resonator coherence times are sufficiently long compared to the operation times guaranteed by the condition $\chi \gg \langle \hat{a}^\dagger \hat{a} \rangle \kappa, \Gamma_\phi, \Gamma_1$, which makes the leakage effects negligible. The experimental value $\chi \sim 2.4$ MHz [54], and the average photon number $\langle \hat{a}^\dagger \hat{a} \rangle \approx 3$ is estimated from simulations data in Fig. 10(d). We note that in systems with shorter-lived modes, such as trapped-ion implementations, mitigating decoherence would indeed be a critical requirement.

VI. CONCLUSION AND OUTLOOK

In this work, we proposed a digital-analog quantum algorithm for simulating the superradiant QPT in the Dicke-Ising model, where individual qubits interact with each other and with a common photon mode. The algorithm features a sequence of analog Jaynes-Cummings gates combined with standard digital single-qubit and two-qubit rotations. This quantum circuit is capable of simulating quench dynamics and the QPT between the normal and superradiant phases. We proposed a protocol based on qubit-parity measurements that allows one to obtain a Schrödinger cat state as the output of resonator Wigner tomography. Additionally, we applied a path-integral description to the model via a bosonic angular representation of the spin operators and formulated the quasiclassical description of fluctuations in the large-spin limit. This approach can be useful for further studies of macroscopic quantum tunneling. Finally, we found that the qubit-qubit interaction leads to an emergent Ising transition driven by the Kibble-Zurek mechanism in imaginary time. The qubit subsystem becomes critical for certain quantum trajectories of the photon field, making the fluctuations in the superradiant phase nontrivial, in contrast to the conventional Dicke model. As an outlook for future investigations in this direction, an interesting question to address is the behavior of the entanglement entropy and the value of the central charge at the QPT and in the superradiant phase.

ACKNOWLEDGMENTS

This work is supported by DPG under Germany's Excellence Strategy–Cluster of Excellence Matter and Light for Quantum Computing (ML4Q) EXC 2004/1 Grant No. 390534769. We further acknowledge support from the German Federal Ministry of Education and Research (BMBF) in the funding program "Quantum technologies–from basic research to market," Contracts No. 13N15584 (project DAQC) and No. 13N16149 (project QSolid). We are also grateful to the funding from the Deutsche Forschungsgemeinschaft (DFG, German Research Foundation) Project ID No. 429529648–TRR 306 QuCoLiMa ("Quantum Cooperativity of Light and Matter"). The authors thank A. Ciani and A. Shnirman for their fruitful discussions.

DATA AVAILABILITY

The data that support the findings of this article are openly available [52].

APPENDIX A: MEAN-FIELD FREE ENERGY FOR DICKE-ISING HAMILTONIAN AT $\omega_z = 0$

In this part of the Appendix, we derive the free energy (20) from the Hamiltonian (1) assuming $\omega_z = 0$. In the limit of zero ω_z, only two types of spin operators remain in the Hamiltonian, σ_q^x and $\sigma_q^z \sigma_{q+1}^z$. Applying the Jordan-Wigner representation to them gives

$$\begin{aligned} \hat{\sigma}_q^x &= \hat{c}_q^\dagger \hat{c}_q - \hat{c}_q \hat{c}_q^\dagger, \\ \hat{\sigma}_q^z \hat{\sigma}_{q+1}^z &= \hat{c}_q^\dagger \hat{c}_{q+1} + \hat{c}_{q+1}^\dagger \hat{c}_q + \hat{c}_q^\dagger \hat{c}_{q+1}^\dagger + \hat{c}_{q+1} \hat{c}_q. \end{aligned} \tag{A1}$$

The Hamiltonian (1) after this transformation has bilinear fermion combinations

$$\begin{aligned} \hat{H}_{\mathrm{DI}} = \omega_0 \hat{a}^\dagger \hat{a} - J \sum_{q=1}^{N} (\hat{c}_q^\dagger \hat{c}_{q+1} + \hat{c}_{q+1}^\dagger \hat{c}_q + \hat{c}_q^\dagger \hat{c}_{q+1}^\dagger + \hat{c}_{q+1} \hat{c}_q) \\ + \frac{g}{\sqrt{N}} (\hat{a}^\dagger + \hat{a}) \sum_{q=1}^{N} (\hat{c}_q^\dagger \hat{c}_q - \hat{c}_q \hat{c}_q^\dagger). \end{aligned} \tag{A2}$$

We note that for $\omega_z \neq 0$ additional terms $\sim \hat{\sigma}_q^z$ arise, yielding nonlocal fermion strings and resulting in a more complicated derivation of the free energy. Consider the partition function $Z = \mathrm{tr}(e^{-\hat{H}_{\mathrm{DI}}/T})$ at finite temperature T. It is reduced to the Matsubara path integral

$$Z = \int d[a, \bar{a}, c, \bar{c}] e^{-S[a,\bar{a},c,\bar{c}]} \tag{A3}$$

over complex boson fields $a(\tau), \bar{a}(\tau)$ and Grassmann fields $c_q(\tau), \bar{c}_q(\tau)$, where τ is the imaginary time $\tau \in [0, 1/T]$. These fields describe, respectively, photons and Jordan-Wigner fermions. The Matsubara action in (A3) is

$$S = \int_0^{1/T} d\tau \left(\bar{a} \partial_\tau a + \sum_{q=1}^{N} \bar{c} \partial_\tau c + H_{\mathrm{DI}}[a, \bar{a}, c, \bar{c}] \right). \tag{A4}$$

Assuming periodic boundary conditions for the Ising chain, we introduce the wave numbers $\mathbf{k} = \frac{2\pi n}{N} - \pi$ with $0 \leqslant n < N$ spanning a Brillouin zone. The Fourier transformation into $\mathbf{k}$ space for Grassmann fields reads as $c_\mathbf{k} = \frac{1}{\sqrt{N}} \sum_{q=1}^{N} e^{-i\mathbf{k}q} c_q$. The action (A4) can be parametrized via Nambu vectors $\Psi_\mathbf{k} = [c_\mathbf{k} \quad \bar{c}_{-\mathbf{k}}]^T$ in γ space resulting in the following form:

$$S = S_{\mathrm{ph}} - \frac{1}{2} \sum_{\mathbf{k}} \int_0^{1/T} d\tau \, \Psi_{-\mathbf{k}}^T \gamma_x G_\mathbf{k}^{-1}[a, \bar{a}] \Psi_\mathbf{k}, \tag{A5}$$

where the inverted Green function (Lagrangian) reads as

$$-G_\mathbf{k}^{-1}[a(\tau), \bar{a}(\tau)] = \begin{bmatrix} \partial_\tau - 2J \cos \mathbf{k} + 2g[\bar{a}(\tau) + a(\tau)]/\sqrt{N} & -2iJ \sin \mathbf{k} \\ 2iJ \sin \mathbf{k} & \partial_\tau + 2J \cos \mathbf{k} - 2g[\bar{a}(\tau) + a(\tau)]/\sqrt{N} \end{bmatrix} \tag{A6}$$

and

$$S_{\rm ph} = \int_0^{1/T} d\tau\,(\bar{a}\partial_\tau a + \omega_0 \bar{a} a) \tag{A7}$$

is the free-photon action. Note that $G_{\mathbf{k}}^{-1}[a,\bar{a}]$ is a nonstationary matrix because of time-depending a fields and, therefore, an inversion is a nontrivial task. Below we tackle this problem in a mean-field approximation.

We parametrize the complex $\bar{a}$ and a through real fields u and v,

$$a(\tau) = \sqrt{N}\frac{u(\tau)+iv(\tau)}{2}, \quad \bar{a}(\tau) = \sqrt{N}\frac{u(\tau)-iv(\tau)}{2}. \tag{A8}$$

After a Fourier transformation defined as $a(\tau) = \sum_n a_n e^{-i2\pi nT\tau}$ and $\bar{a}(\tau) = \sum_n a_n e^{i2\pi nT\tau}$, we take the Gaussian integrals over real boson v_n and real Grassmann $\Psi_{\mathbf{k}}$ fields. As a result, we receive an effective action for the real boson $u(\tau)$, which is a sum of the free-boson action S_u and the spin contribution given by the logarithm of the fermion determinant,

$$S_{\rm eff} = \frac{1}{4}N\int_0^{1/T}\left(\frac{1}{\omega_0}(\partial_\tau u)^2 + \omega_0 u^2\right)d\tau - \frac{1}{2}\ln\det\left(-G_{\mathbf{k}}^{-1}[u]\right). \tag{A9}$$

It features the inverted Green function (A6) written as $G_{\mathbf{k}}^{-1}[u] = -\gamma_0\partial_\tau - H_{\mathbf{k}}(\tau)$, where the τ-dependent Hamiltonian matrix in Nambu γspace reads as

$$H_{\mathbf{k}}(\tau) = -2J(\gamma_z\cos\mathbf{k} - \gamma_y\sin\mathbf{k}) + 2g\gamma_z u(\tau). \tag{A10}$$

In the mean-field approximation, we assume $u(\tau) = \text{const}$ neglecting temporal fluctuations. The fermion determinant in (A9) can be found analytically through an infinite product over Matsubara frequencies with 2×2 γ-matrix determinants,

$$\ln\det\left(G_{\mathbf{k}}^{-1}[u]G_{\mathbf{k}}[0]\right) = N\int_{-\pi}^{\pi}\frac{d\mathbf{k}}{2\pi}\ln\left(\prod_n \frac{\det_\gamma[-i2\pi nT\gamma_0 - 2J(\gamma_z\cos\mathbf{k} - \gamma_y\sin\mathbf{k}) + 2g\gamma_z u]}{\det_\gamma[-i2\pi nT\gamma_0 - 2J(\gamma_z\cos\mathbf{k} - \gamma_y\sin\mathbf{k})]}\right). \tag{A11}$$

We added $G_{\mathbf{k}}[0]$ to regularize the action. This factor emerges from normalizing the partition sum by its value at $g = 0$. To compute the infinite product we use the identity

$$\prod_{n\geqslant 1}(1 + x^2/n^2) = \frac{1}{\pi\sqrt{x}}\sinh(\pi|x|). \tag{A12}$$

Taking the leading term $\sim\frac{1}{T}$ in the limit of low temperatures, and then integrating over $\mathbf{k}$, we arrive at the mean-field action

$$S_{\rm mf} = N\int_0^{1/T}\left(\frac{(\partial_\tau u)^2}{4\omega_0} + \mathcal{F}(u)\right)d\tau \tag{A13}$$

with the normalized free energy $\mathcal{F}(u) = \frac{1}{N}F_{\rm DI}(u)$ provided in Eq. (21),

$$\mathcal{F}(u) = \frac{1}{4}\omega_0 u^2 - \frac{2}{\pi}(J + g|u|)\mathrm{E}\left[\frac{4gJ|u|}{(J+g|u|)^2}\right]. \tag{A14}$$

APPENDIX B: INSTANTON TRAJECTORY

Consider the mean-field part of the action (A13). When the system is in the superradiant phase, a variation of $S_{\rm mf}$ by u yields the equation for an instanton saddle-point trajectory,

$$\partial_\tau^2 u - 2\omega_0\partial_u\mathcal{F}(u) = 0, \tag{B1}$$

with boundary conditions $u(\tau = 0) = -u(\tau = 1/T) = -u_0$, where $u_0 > 0$ is a nonzero solution of the equation $\partial_u\mathcal{F}(u) = 0$ for the superradiant order parameter. There is also an integral motion, which is analogous to the full energy in classical mechanics. It reads as

$$-\frac{(\partial_\tau u)^2}{4\omega_0} + \mathcal{F}(u) = \mathcal{F}(-u_0), \tag{B2}$$

where the constant $\mathcal{F}(-u_0)$ is given by the free-energy minimum at $u = -u_0$. The instanton solution is given by an *implicit* function $u_{\rm inst}(\tau)$, which follows from Eq. (B2) as

$$\tau = \int_{-u_0}^{u_{\rm inst}(\tau)}\frac{du}{\sqrt{2\omega_0[\mathcal{F}(u) - \mathcal{F}(-u_0)]}}. \tag{B3}$$

The schematic shape of the solution that follows from this integral is presented in Fig. 3(c).

APPENDIX C: DERIVATION OF THE CIRCUIT STRUCTURE

In this appendix, we comment on the derivation of the Rabi gate (48) and the sequence of gates (61) that simulate the evolution of the Dicke-Ising model. We begin with the Rabi model. For its Trotterized evolution operator

$$\hat{U}_{\rm R}(t) = \prod_{k=1}^{N}\hat{U}_{\rm R}(t_{k+1}, t_k), \quad t_k = (k-1)\Delta t, \tag{C1}$$

each step is approximated by a sequence of three evolutions governed by the JC Hamiltonian (47), as shown in Eq. (53) of the main text. It is advantageous to rewrite this equation in the following form:

$$\hat{U}_{\rm R}(t_{k+1}, t_k) = \hat{U}_{\rm JC}\left(t_k + \Delta t, t_k + \tfrac{3}{4}\Delta t\right)\hat{\sigma}^x\,\hat{U}_{\rm JC}\left(t_k + \tfrac{3}{4}\Delta t, t_k + \tfrac{1}{4}\Delta t\right)\hat{\sigma}^x\,\hat{U}_{\rm JC}\left(t_k + \tfrac{1}{4}\Delta t, t_k\right), \tag{C2}$$

where $\hat{U}_{\rm JC}(t)$ denotes the evolution operator of the JC model.

Our goal is to relate this Trotterized evolution to a sequence of quantum gates that can be implemented on quantum hardware, including the JC gate (48) introduced in the main text. To this end, we switch to the interaction picture with respect to the free Hamiltonian $\hat{H}_0$ [see Eqs.(52) and (54)]. Using the identity

$$e^{i\hat{H}_0 t}\hat{U}_{\rm JC}(t, t')e^{-i\hat{H}_0 t'} = \hat{S}_{\rm JC}(\theta), \quad \theta = g(t - t'), \tag{C3}$$

we find that the above unitary transformation of $\hat{U}_{\rm JC}$ yields the JC gate (48) with the phase determined by a product of the time interval and the strength of interaction. Applying this to the full Trotterized step (C2), we obtain

$$\begin{aligned}\hat{S}_{\rm R}(t_{k+1},t_k) &:= e^{i\hat{H}_0 t_{k+1}}\hat{U}_{\rm R}(t_{k+1},t_k)e^{-i\hat{H}_0 t_k}\\ &= \hat{S}_{\rm JC}(\theta/2)\hat{X}_\pi(\varphi_+)\hat{S}_{\rm JC}(\theta)\hat{X}_\pi(\varphi_-)\hat{S}_{\rm JC}(\theta/2),\end{aligned} \tag{C4}$$

where the rotated X gates $\hat{X}_\pi(\varphi_\pm)$ are defined in Eq. (56) with phases $\varphi_- = \omega_0(t_k + \Delta t/4)$ and $\varphi_+ = \omega_0(t_k + 3\Delta t/4)$. These arise from expressing the Pauli $\hat{\sigma}^x$ operators in the rotating frame:

$$\begin{aligned}\hat{X}_\pi(\varphi_+) &= e^{-\frac{i}{2}\omega_0(t_k+\frac{3}{4}\Delta t)\hat{\sigma}^z}\hat{\sigma}^x e^{\frac{i}{2}\omega_0(t_k+\frac{3}{4}\Delta t)\hat{\sigma}^z}\\ &\equiv \exp(-i\varphi_+\hat{\sigma}^z)\hat{\sigma}^x,\end{aligned} \tag{C5}$$

with a similar expression for $\hat{X}_\pi(\varphi_-)$. In this way, we have derived the unitary gate (55), which emulates a single Trotter step of the Rabi model in the rotating frame.

Let us now discuss how the gate sequence (60), which approximates the evolution of the Dicke-Ising model, can be justified. To this end, we begin by describing the construction of the Dicke gate $\hat{S}_{\rm D}$, defined in Eq. (61), in the case of two spins. It will become clear that a generalization to the case with an arbitrary number of spins N is straightforward. For $N = 2$, we rewrite the Dicke Hamiltonian as a sum of three terms:

$$\begin{aligned}&\hat{H}_{\rm D} = \hat{H}^{(1)} + \hat{H}^{(2)} - \hat{h}_0, \quad \hat{H}^{(j)} = \hat{h}_0 + g(\hat{a} + \hat{a}^\dagger)\hat{\sigma}_j^x,\\ &\hat{h}_0 = \omega_0\hat{a}^\dagger\hat{a}.\end{aligned} \tag{C6}$$

This decomposition naturally suggests a Trotterization scheme of the form

$$\hat{U}_{\rm D}(t_{k+1},t_k) \approx \hat{U}_{\rm R}^{(2)}(t_k+\Delta t,t_k)\, e^{i\hat{h}_0\Delta t}\, \hat{U}_{\rm R}^{(1)}(t_k+\Delta t,t_k), \tag{C7}$$

where each $\hat{U}_{\rm R}^{(j)}$ denotes the evolution operator generated by the Rabi Hamiltonian $\hat{H}^{(j)}$. For these, we apply the same approximation as previously used [see Eq. (C2)]. It is important to emphasize that there are multiple ways to Trotterize the evolution operator corresponding to $\hat{H}_{\rm D}$. Our specific choice of Trotterization is motivated by its favorable error properties: the discretization error scales as $O(\Delta t^3)$, which matches that of the Rabi gate (55).

It is now instructive to move to the rotating frame defined by the free-bosonic Hamiltonian $\hat{h}_0$. Let us denote evolution operators in this frame by $\widetilde{S}(t,t')$, in contrast to $\hat{S}(t,t')$, which refers to the interaction representation with respect to the Hamiltonian $\hat{H}_0$ used in the main text. Noting that $e^{i\hat{h}_0\Delta t} \equiv \hat{U}_0(t_k, t_k+\Delta t)$ represents backward time evolution under the free Hamiltonian, we can deduce from Eq. (C7) the following relation:

$$\widetilde{S}_{\rm D}(t_{k+1},t_k) = \widetilde{S}_{\rm R}^{(2)}(t_k+\Delta t,t_k)\widetilde{S}_{\rm R}^{(1)}(t_k+\Delta t,t_k). \tag{C8}$$

Here, the Rabi gates in the new rotating frame are related to the basic gates (55) by simple Z rotations:

$$\begin{aligned}\widetilde{S}_{\rm R}^{(j)}(t_k+\Delta t,t_k) &= e^{\frac{i}{2}\phi_{k+1}\hat{\sigma}_j^z}\hat{S}_{\rm R}^{(j)}(t_k+\Delta t,t_k)e^{-\frac{i}{2}\phi_k\hat{\sigma}_j^z},\\ \phi_k &= \omega_0 t_k.\end{aligned} \tag{C9}$$

The same applies to the full gate $\widetilde{S}_{\rm D}$. This gate differs from its counterpart $\hat{S}_{\rm D}$ by a similarity transformation, consisting of Z rotations acting on both spins. Consequently, the structure of Eq. (C8) also holds in the rotating frame defined with respect to $\hat{H}_0$:

$$\hat{S}_{\rm D}(t_{k+1},t_k) = \hat{S}_{\rm R}^{(2)}(t_k+\Delta t,t_k)\hat{S}_{\rm R}^{(1)}(t_k+\Delta t,t_k). \tag{C10}$$

Thus, we have arrived at the result (61), provided the qubit-boson architecture permits interactions between any qubit and the resonator. In the case of restricted connectivity, SWAP gates must be used, leading to the equivalent expression:

$$\begin{aligned}&\hat{S}_{\rm D}(t_{k+1},t_k)\\ &\quad= \mathrm{SWAP}^{(12)}\hat{S}_{\rm R}^{(1)}(t_k+\Delta t,t_k)\mathrm{SWAP}^{(12)}\hat{S}_{\rm R}^{(1)}(t_k+\Delta t,t_k).\end{aligned} \tag{C11}$$

The above considerations can be readily extended to the case of an arbitrary number of qubits N. Indeed, the Dicke Hamiltonian can be rewritten as follows:

$$\hat{H}_{\rm D} = \sum_{j=1}^{N}\hat{H}^{(j)} - (N-1)\hat{h}_0, \tag{C12}$$

and the corresponding Trotterization scheme takes the form

$$\hat{U}_{\rm D}(t_{k+1},t_k) \approx \hat{U}^{(N)}(t_k+\Delta t,t_k)\prod_{j=1}^{N-1} e^{i\hat{h}_0\Delta t}\,\hat{U}^{(j)}(t_k+\Delta t,t_k), \tag{C13}$$

which is a straightforward generalization of Eq. (C7). The result (61) from the main text then follows by applying the same reasoning as in the case of $N = 2$.

It remains to discuss how the Ising-type terms in the Hamiltonian (1) can be incorporated into the above Trotterized scheme. To justify the appearance of Z and ZZ gates in Eq. (60), we assume that the Ising Hamiltonian is applied during the time interval $[t_k+\Delta t, t_k]$ in the form of δ pulses:

$$\begin{aligned}&\hat{H}(t) = \hat{H}_{\rm D} - \eta\,\delta(t-t_{k+1})\sum_{j=1}^{N-1}\hat{\sigma}_j^z\hat{\sigma}_{j+1}^z - \beta\,\delta(t-t_{k+1})\sum_{j=1}^{N}\hat{\sigma}_j^z,\\ &\eta = J\Delta t, \quad \beta = \omega_z\Delta t,\end{aligned} \tag{C14}$$

so that the dynamics depends only on the effective phases η and β. This ansatz corresponds to a separate Trotterization of the Dicke and Ising Hamiltonians and directly leads to the gate sequence given in Eq. (60).

APPENDIX D: MODEL OF A DISSIPATION IN THE CIRCUIT

In the emulation of noise effects upon Trotterization, we apply Lindbladian dissipative dynamics after each of the L unitariy $\hat{S}_{\rm DI}$ gates. This model of noise takes into account dephasing (Γ_ϕ) and relaxation (Γ_1) rates of the qubits, and assumes Rabi gate duration *physical* time $\tau_{\rm Rabi}$. When a qubit is detuned from the resonator, it is assumed to remain fully coherent. Photon relaxation during a single $\hat{S}_{\rm DI}$ gate occurs at a rate κ at a time interval $N\tau_{\rm R}$, due to N Rabi gates being applied sequentially. We do not account for errors introduced by CNOT or SWAP gates; their operation times are also omitted from the noise model.

Consider the first Trotter step where the initial state $\hat{\rho}_0 = |\mathrm{FM}\rangle\langle\mathrm{FM}|$ evolves into a mixed state $\hat{\rho}_1$. This step proceeds as follows: (i) a unitary transformation is applied to obtain $\hat{\rho}_0' = \hat{S}_{\mathrm{DI}}\hat{\rho}_0\hat{S}_{\mathrm{DI}}^{\dagger}$, (ii) the state $\hat{\rho}_0'$ then undergoes dissipative evolution according to the Lindblad master equation

$$\frac{d\hat{\rho}}{dt} = N\kappa\left(\hat{a}\hat{\rho}\hat{a}^{\dagger} - \frac{1}{2}\{\hat{a}^{\dagger}\hat{a},\hat{\rho}\}\right) + \frac{\Gamma_{\phi}}{2}\sum_j\left(\hat{\sigma}_j^z\hat{\rho}\hat{\sigma}_j^z - \hat{\rho}\right) + \Gamma_1\sum_j\left(\hat{\sigma}_j^-\hat{\rho}\hat{\sigma}_j^+ - \frac{1}{2}\{\hat{\sigma}_j^+\hat{\sigma}_j^-,\hat{\rho}\}\right). \tag{D1}$$

The evolution governed by this equation is applied for a time interval τ_{R}, transforming $\hat{\rho}_0'$ into $\hat{\rho}_1$. The prefactor N in front of κ reflects that fact that the Rabi gate is applied N times to the resonator.

[1] C. F. Lee and N. F. Johnson, First-order superradiant phase transitions in a multiqubit cavity system, Phys. Rev. Lett. **93**, 083001 (2004).

[2] S. Gammelmark and K. Mølmer, Phase transitions and Heisenberg limited metrology in an Ising chain interacting with a single-mode cavity field, New J. Phys. **13**, 053035 (2011).

[3] Y. Zhang, L. Yu, J. Q. Liang, G. Chen, S. Jia, and F. Nori, Quantum phases in circuit QED with a superconducting qubit array, Sci. Rep. **4**, 4083 (2014).

[4] J. Gelhausen, M. Buchhold, A. Rosch, and P. Strack, Quantum-optical magnets with competing short- and long-range interactions: Rydberg-dressed spin lattice in an optical cavity, SciPost Phys. **1**, 004 (2016).

[5] J. Rohn, M. Hörmann, C. Genes, and K. P. Schmidt, Ising model in a light-induced quantized transverse field, Phys. Rev. Res. **2**, 023131 (2020).

[6] A. Schellenberger and K. P. Schmidt, (Almost) everything is a dicke model-mapping non-superradiant correlated light-matter systems to the exactly solvable Dicke model, SciPost Phys. Core **7**, 038 (2024).

[7] A. Langheld, M. Hörmann, and K. P. Schmidt, Quantum phase diagrams of Dicke-Ising models by a wormhole algorithm, arXiv:2409.15082.

[8] T. O. Puel and T. Macrì, Confined meson excitations in rydberg-atom arrays coupled to a cavity field, Phys. Rev. Lett. **133**, 106901 (2024).

[9] V. N. Popov and S. A. Fedotov, The functional-integration method and diagram technique for spin systems, Zh. Eksp. Teor. Fiz. **94**, 183 (1988).

[10] C. Emary and T. Brandes, Chaos and the quantum phase transition in the dicke model, Phys. Rev. E **67**, 066203 (2003).

[11] P. R. Eastham and P. B. Littlewood, Bose condensation of cavity polaritons beyond the linear regime: The thermal equilibrium of a model microcavity, Phys. Rev. B **64**, 235101 (2001).

[12] E. G. Dalla Torre, S. Diehl, M. D. Lukin, S. Sachdev, and P. Strack, Keldysh approach for nonequilibrium phase transitions in quantum optics: Beyond the Dicke model in optical cavities, Phys. Rev. A **87**, 023831 (2013).

[13] E. G. Dalla Torre, Y. Shchadilova, E. Y. Wilner, M. D. Lukin, and E. Demler, Dicke phase transition without total spin conservation, Phys. Rev. A **94**, 061802(R) (2016).

[14] P. Kirton, M. M. Roses, J. Keeling, and E. G. Dalla Torre, Introduction to the Dicke model: From equilibrium to nonequilibrium, and vice versa, Adv. Quantum Technol. **2**, 1800043 (2019).

[15] D. S. Shapiro, W. V. Pogosov, and Y. E. Lozovik, Universal fluctuations and squeezing in a generalized Dicke model near the superradiant phase transition, Phys. Rev. A **102**, 023703 (2020).

[16] F. Dimer, B. Estienne, A. S. Parkins, and H. J. Carmichael, Proposed realization of the dicke-model quantum phase transition in an optical cavity QED system, Phys. Rev. A **75**, 013804 (2007).

[17] P. Nataf and C. Ciuti, Vacuum degeneracy of a circuit QED system in the ultrastrong coupling regime, Phys. Rev. Lett. **104**, 023601 (2010).

[18] O. Viehmann, J. von Delft, and F. Marquardt, Superradiant phase transitions and the standard description of circuit QED, Phys. Rev. Lett. **107**, 113602 (2011).

[19] K. Baumann, C. Guerlin, F. Brennecke, and T. Esslinger, Dicke quantum phase transition with a superfluid gas in an optical cavity, Nature (London) **464**, 1301 (2010).

[20] X.-F. Zhang, Q. Sun, Y.-C. Wen, W.-M. Liu, S. Eggert, and A.-C. Ji, Rydberg polaritons in a cavity: A superradiant solid, Phys. Rev. Lett. **110**, 090402 (2013).

[21] M. P. Baden, K. J. Arnold, A. L. Grimsmo, S. Parkins, and M. D. Barrett, Realization of the Dicke model using cavity-assisted Raman transitions, Phys. Rev. Lett. **113**, 020408 (2014).

[22] J. Klinder, H. Keßler, M. Wolke, L. Mathey, and A. Hemmerich, Dynamical phase transition in the open Dicke model, Proc. Natl. Acad. Sci. USA **112**, 3290 (2015),.

[23] A. Safavi-Naini, R. J. Lewis-Swan, J. G. Bohnet, M. Gärttner, K. A. Gilmore, J. E. Jordan, J. Cohn, J. K. Freericks, A. M. Rey, and J. J. Bollinger, Verification of a many-ion simulator of the Dicke model through slow quenches across a phase transition, Phys. Rev. Lett. **121**, 040503 (2018).

[24] J. Klinder, H. Keßler, M. R. Bakhtiari, M. Thorwart, and A. Hemmerich, Observation of a superradiant Mott insulator in the Dicke-Hubbard model, Phys. Rev. Lett. **115**, 230403 (2015).

[25] G. Ferioli, A. Glicenstein, I. Ferrier-Barbut, and A. Browaeys, A non-equilibrium superradiant phase transition in free space, Nat. Phys. **19**, 1345 (2023).

[26] C. Liedl, F. Tebbenjohanns, C. Bach, S. Pucher, A. Rauschenbeutel, and P. Schneeweiss, Observation of superradiant bursts in a cascaded quantum system, Phys. Rev. X **14**, 011020 (2024).

[27] J. M. Fink, R. Bianchetti, M. Baur, M. Göppl, L. Steffen, S. Filipp, P. J. Leek, A. Blais, and A. Wallraff, Dressed collective qubit states and the Tavis-Cummings model in circuit QED, Phys. Rev. Lett. **103**, 083601 (2009).

[28] M. Feng, Y. P. Zhong, T. Liu, L. L. Yan, W. L. Yang, J. Twamley, and H. Wang, Exploring the quantum critical behavior in a driven Tavis–Cummings circuit, Nat. Commun. **6**, 7111 (2015).

[29] F. Yoshihara, T. Fuse, S. Ashhab, K. Kakuyanagi, S. Saito, and K. Semba, Superconducting qubit–oscillator circuit beyond the ultrastrong-coupling regime, Nat. Phys. **13**, 44 (2017).

[30] P. Forn-Díaz, L. Lamata, E. Rico, J. Kono, and E. Solano, Ultrastrong coupling regimes of light-matter interaction, Rev. Mod. Phys. **91**, 025005 (2019).

[31] A. Frisk Kockum, A. Miranowicz, S. De Liberato, S. Savasta, and F. Nori, Ultrastrong coupling between light and matter, Nat. Rev. Phys. **1**, 19 (2019).

[32] A. Blais, A. L. Grimsmo, S. M. Girvin, and A. Wallraff, Circuit quantum electrodynamics, Rev. Mod. Phys. **93**, 025005 (2021).

[33] W. Qin, A. F. Kockum, C. S. Muñoz, A. Miranowicz, and F. Nori, Quantum amplification and simulation of strong and ultrastrong coupling of light and matter, Phys. Rep. **1078**, 1 (2024).

[34] R. P. Feynman, Simulating physics with computers, Int. J. Theor. Phys. **21**, 467 (1982).

[35] S. Lloyd, Universal quantum simulators, Science **273**, 1073 (1996).

[36] H. Weimer, M. Müller, I. Lesanovsky, P. Zoller, and H. P. Büchler, A Rydberg quantum simulator, Nat. Phys. **6**, 382 (2010).

[37] L. Bassman Oftelie, M. Urbanek, M. Metcalf, J. Carter, A. F. Kemper, and W. A. de Jong, Simulating quantum materials with digital quantum computers, Quantum Sci. Technol. **6**, 043002 (2021).

[38] S. Bravyi, A. W. Cross, J. M. Gambetta, D. Maslov, P. Rall, and T. J. Yoder, High-threshold and low-overhead fault-tolerant quantum memory, Nature (London) **627**, 778 (2024).

[39] A. Miessen, D. J. Egger, I. Tavernelli, and G. Mazzola, Benchmarking digital quantum simulations above hundreds of qubits using quantum critical dynamics, PRX Quantum **5**, 040320 (2024).

[40] B. Fauseweh, Quantum many-body simulations on digital quantum computers: State-of-the-art and future challenges, Nat. Commun. **15**, 2123 (2024).

[41] A. Macridin, P. Spentzouris, J. Amundson, and R. Harnik, Electron-phonon systems on a universal quantum computer, Phys. Rev. Lett. **121**, 110504 (2018).

[42] A. Macridin, P. Spentzouris, J. Amundson, and R. Harnik, Digital quantum computation of fermion-boson interacting systems, Phys. Rev. A **98**, 042312 (2018).

[43] A. Mezzacapo, U. Las Heras, J. S. Pedernales, L. DiCarlo, E. Solano, and L. Lamata, Digital quantum Rabi and Dicke models in superconducting circuits, Sci. Rep. **4**, 7482 (2014).

[44] N. K. Langford, R. Sagastizabal, M. Kounalakis, C. Dickel, A. Bruno, F. Luthi, D. J. Thoen, A. Endo, and L. DiCarlo, Experimentally simulating the dynamics of quantum light and matter at deep-strong coupling, Nat. Commun. **8**, 1715 (2017).

[45] Y. Liu, S. Singh, K. C. Smith, E. Crane, J. M. Martyn, A. Eickbusch, A. Schuckert, R. D. Li, J. Sinanan-Singh, M. B. Soley, T. Tsunoda, I. L. Chuang, N. Wiebe, and S. M. Girvin, Hybrid oscillator-qubit quantum processors: Instruction set architectures, abstract machine models, and applications, PRX Quantum (2025).

[46] S. Kumar, N. N. Hegade, A.-M. Visuri, B. A. Bhargava, J. F. R. Hernandez, E. Solano, F. Albarrán-Arriagada, and G. A. Barrios, Digital-analog quantum computing of fermion-boson models in superconducting circuits, npj Quantum Inf. **11**, 43 (2025).

[47] G. Huber, F. Roy, L. Koch, I. Tsitsilin, J. Schirk, N. Glaser, N. Bruckmoser, C. Schweizer, J. Romeiro, G. Krylov, M. Singh, F. Haslbeck, M. Knudsen, A. Marx, F. Pfeiffer, C. Schneider, F. Wallner, D. Bunch, L. Richard, L. Södergren, K. Liegener, M. Werninghaus, and S. Filipp, Parametric multielement coupling architecture for coherent and dissipative control of superconducting qubits, PRX Quantum **6**, 030313 (2025).

[48] M. Reagor, W. Pfaff, C. Axline, R. W. Heeres, N. Ofek, K. Sliwa, E. Holland, C. Wang, J. Blumoff, K. Chou, M. J. Hatridge, L. Frunzio, M. H. Devoret, L. Jiang, and R. J. Schoelkopf, Quantum memory with millisecond coherence in circuit QED, Phys. Rev. B **94**, 014506 (2016).

[49] S. Ganjam, Y. Wang, Y. Lu, A. Banerjee, C. U. Lei, L. Krayzman, K. Kisslinger, C. Zhou, R. Li, Y. Jia, M. Liu, L. Frunzio, and R. J. Schoelkopf, Surpassing millisecond coherence in on chip superconducting quantum memories by optimizing materials and circuit design, Nat. Commun. **15**, 3687 (2024).

[50] M. Um, J. Zhang, D. Lv, Y. Lu, S. An, J.-N. Zhang, H. Nha, M. S. Kim, and K. Kim, Phonon arithmetic in a trapped ion system, Nat. Commun. **7**, 11410 (2016).

[51] Y. Wang, S. Crain, C. Fang, B. Zhang, S. Huang, Q. Liang, P. H. Leung, K. R. Brown, and J. Kim, High-fidelity two-qubit gates using a microelectromechanical-system-based beam steering system for individual qubit addressing, Phys. Rev. Lett. **125**, 150505 (2020).

[52] D. S. Shapiro, Y. Weber, T. Bode, F. K. Wilhelm, and D. Bagrets, Data for digital-analog simulations of schrödinger cat states in the Dicke-Ising model, https://zenodo.org/records/16581022.

[53] Z. Leghtas, G. Kirchmair, B. Vlastakis, M. H. Devoret, R. J. Schoelkopf, and M. Mirrahimi, Deterministic protocol for mapping a qubit to coherent state superpositions in a cavity, Phys. Rev. A **87**, 042315 (2013).

[54] B. Vlastakis, G. Kirchmair, Z. Leghtas, S. E. Nigg, L. Frunzio, S. M. Girvin, M. Mirrahimi, M. H. Devoret, and R. J. Schoelkopf, Deterministically encoding quantum information using 100-Photon Schrödinger cat states, Science **342**, 607 (2013).

[55] A. Grimm, N. E. Frattini, S. Puri, S. O. Mundhada, S. Touzard, M. Mirrahimi, S. M. Girvin, S. Shankar, and M. H. Devoret, Stabilization and operation of a Kerr-cat qubit, Nature (London) **584**, 205 (2020).

[56] R. Lescanne, M. Villiers, T. Peronnin, A. Sarlette, M. Delbecq, B. Huard, T. Kontos, M. Mirrahimi, and Z. Leghtas, Exponential suppression of bit-flips in a qubit encoded in an oscillator, Nat. Phys. **16**, 509 (2020).

[57] Y. Xu, D. Fallas Padilla, and H. Pu, Multicriticality and quantum fluctuation in a generalized Dicke model, Phys. Rev. A **104**, 043708 (2021).

[58] Y. Salathé, M. Mondal, M. Oppliger, J. Heinsoo, P. Kurpiers, A. Potočnik, A. Mezzacapo, U. Las Heras, L. Lamata, E. Solano, S. Filipp, and A. Wallraff, Digital quantum simulation of spin models with circuit quantum electrodynamics, Phys. Rev. X **5**, 021027 (2015).

[59] D. Wecker, M. B. Hastings, N. Wiebe, B. K. Clark, C. Nayak, and M. Troyer, Solving strongly correlated electron models on a quantum computer, Phys. Rev. A **92**, 062318 (2015).

[60] L. G. Lutterbach and L. Davidovich, Method for direct measurement of the Wigner function in cavity QED and ion traps, Phys. Rev. Lett. **78**, 2547 (1997).